

1 **Microphysical properties of various precipitation systems worldwide**
2 **classified via objective methods based on dual-frequency precipitation**
3 **radar observations**

4 Yujia Zhang^{1,2} Xiaodong Zhang^{1,2}, Xiang Ni^{1,2}

5 ¹Chongqing Jinpo Mountain Karst Ecosystem National Observation and Research Station, School of Geographical Sciences,
6 Southwest University, Chongqing, China

7 ²Chongqing Engineering Research Center for Remote Sensing Big Data Application, School of Geographical Sciences,
8 Southwest University, Chongqing, China

9 *Correspondence to:* Xiang Ni (nixiang@swu.edu.cn)

10

11 **Abstract.** Microphysical properties play crucial roles in physical processes related to the development of precipitation. In this
12 study, Global Precipitation Measurement (GPM) dual-frequency precipitation radar (DPR) data were processed to demonstrate
13 the microphysical properties of different precipitation systems (~~PSs~~PS) that are objectively classified with the k-means
14 clustering algorithm. Four types of regular/non-extreme ~~PSs~~PS (high-latitude shallow ~~PSs~~PS, subtropical shallow ~~PSs~~PS,
15 moderate ~~PSs~~PS, deep ~~PSs~~PS) and four types of extreme ~~PSs~~PS (extreme deep ~~PSs~~PS, strong ~~PSs~~PS, extreme strong ~~PSs~~PS, and
16 marine extreme ~~PSs~~PS) were recognized. These eight types of ~~PSs~~PS exhibit differences in spatial-temporal features and
17 convection characteristics, such as storm height, rain intensity, and vertical structures. For example, the extreme strong ~~PSs~~PS,
18 with the highest radar echo top and largest mean mass-weighted mean diameter are mainly located over tropical continents,
19 ~~mainly locate over tropical continent~~, whereas high-latitude shallow ~~PSs~~PS have the least precipitation rate and mean
20 normalized intercept parameter values. The relationships between convection features and microphysical properties also vary
21 among the eight types of ~~PSs~~PSs. For extreme ~~PSs~~PS, maximum precipitation rate near the surface generally exceeds 100 mm
22 h⁻¹ and balanced breakup and coalescence processes play a dominant role compared with non-extreme ~~PSs~~PS. In
23 ~~contrary~~contrast, the coalescence processes dominate near the surface in two types of shallow ~~PSs~~PS. These results highlight
24 the diversity of global precipitation microphysics and emphasize the necessity of global studies to increase the understanding
25 of precipitation processes.

26

27 1. Introduction

28 The microphysical characteristics of precipitation provide crucial information for describing precipitation. The deficiency of
29 precipitation microphysical parameterization schemes is a significant factor contributing to precipitation errors in weather and
30 climate models (Snook and Xue, 2008). Accurately obtaining spatiotemporal variations in precipitation microphysical
31 parameters is essential for understanding the physical processes of precipitation, increasing the accuracy of quantitative
32 precipitation estimation, and evaluating microphysical parameterizations in models (Chen et al., 2011; Zhang et al., 2023).
33 Currently, observations and characteristics of precipitation microphysics at the global scale remain lacking because of the
34 limited number of observation approaches.

35

36 The drop size distribution (DSD) is a typical metric for depicting precipitation microphysics. DSD features can be derived
37 from observations obtained via disdrometers, ground-based radar instruments, and space-based radar instruments. In radar
38 instruments, the interaction of electromagnetic waves with hydrometeors is used to retrieve DSD parameters (Marzuki et al.,
39 2023), whereas disdrometers measure raindrop counts to directly obtain DSDs at the surface. Disdrometers provide only point
40 measurements at specific levels and cannot measure the vertical structure of DSDs. Moreover, disdrometer observations are
41 relatively sparse, especially over the ocean.~~Moreover, disdrometers have not been deployed globally, especially over the ocean.~~
42 Although ground-based radar instruments can measure the three-dimensional structure of precipitation, they can only be used
43 in limited areas, and their observation accuracy is significantly affected by the terrain conditions within the observation area
44 (Dai et al., 2020). In contrast, space-based radar instruments can provide the vertical structures of DSD parameters worldwide.
45 This study focuses on the microphysical characteristics of various precipitation systems (PSsPS) worldwide. Compared with
46 other instruments, space-based radar instruments are the most suitable for researching global precipitation microphysics.

47

48 In 1997, the Tropical Rainfall Measuring Mission (TRMM) satellite was launched by the National Aeronautics and Space
49 Administration (NASA) and the Japan Aerospace Exploration Agency (JAXA). The precipitation radar (PR), which operates
50 in the Ku-band (13.8 GHz), was carried by the TRMM (Iguchi et al., 2000). This marked the beginning of the observation of
51 precipitation microphysics via space-based radar instruments.~~Notably, DSD parameters were retrieved from the radar~~
52 ~~reflectivity measured by the PR with the assumption that the DSD can be characterized by the diameter parameter itself (Iguchi~~
53 ~~et al., 2000). As a result, the DSDs obtained via retrieval exhibited large errors.~~ In 2014, NASA and JAXA successfully
54 launched the Global Precipitation Measurement (GPM) Core Observatory (GPM-CO). The GPM-CO carried the first
55 spaceborne dual-frequency precipitation radar (DPR) system, operating in the Ku and Ka bands (13.6 and 35.5 GHz,
56 respectively) (Skofronick-Jackson et al., 2017). Via the use of this characteristic, mean mass-weighted mean diameter (D_m)
57 and mean normalized intercept parameter (N_w) can be retrieved. The retrieved DSD parameters have been verified with ground-
58 based observations and exhibit closer agreement with in situ measurements than those derived from~~are better than those~~
59 ~~obtained via~~ the TRMM PR algorithm (Sun et al., 2020). In addition, validation studies have confirmed the feasibility of using

60 DPR observations for DSD parameter analysis (D'Adderio et al., 2018; Peinó et al., 2024). Peinó et al. (2024) used
61 observational data from seven Parsivel disdrometers across different topographic zones in the western Mediterranean to
62 validate GPM DSD products. They reported that the GPM DPR products effectively captured the variations in DSDs observed
63 under different rainfall intensities. Therefore, GPM DSD products have been widely employed to investigate the microphysical
64 characteristics of precipitation in the literature (Wen et al., 2024, 2023) .

65

66 However, previous studies involving GPM DSD products have focused mainly on specific locations or weather systems. For
67 example, Li et al. (2024) studied the vertical structure and DSD characteristics of different precipitation types during the rainy
68 season over South China and reported that the precipitation type and intensity affect the DSD parameters. In their study, under
69 the same precipitation intensity, shallow convective precipitation exhibited the smallest D_m and largest N_w values, whereas
70 deep convective precipitation exhibited the opposite phenomenon. Additionally, regarding stratiform precipitation, for
71 ~~Precipitation precipitation Rate-rate~~ $> 3.5 \text{ mm h}^{-1}$, D_m slightly increased, and in regard to shallow convective precipitation, D_m
72 remained at approximately 1.3 mm for Precipitation Rate $> 2 \text{ mm h}^{-1}$. Similarly, Wen et al. (2023) analyzed the seasonal
73 variations in the vertical structure of precipitation microphysics in East China. They reported that the spatial distributions of
74 D_m and N_w demonstrated obvious seasonal variations and that there are more small raindrops in convective precipitation in
75 autumn and winter than during the other seasons. ~~These studies revealed the variations in microphysical characteristics across~~
76 ~~different seasons and rainfall types.~~ Additionally, regarding weather conditions, regional variations in the precipitation
77 characteristics of tropical cyclones have been investigated over the North Indian Ocean (Kumar et al., 2023). Research has
78 revealed that the nature of microphysical processes largely influences the growth of droplets in convective and stratiform rain.
79 Wu et al. (2022) investigated the DSD characteristics of record-breaking Typhoon In-Fa. Their findings revealed significant
80 internal and regional differences in the microphysical characteristics of typhoon precipitation. When different precipitation
81 types during Typhoon In-Fa were compared, convective precipitation (N_w values ranging from 3.80 to $3.96 \text{ m}^{-3} \text{ mm}^{-1}$)
82 exhibited higher raindrop concentrations than did stratiform precipitation (N_w values ranging from 3.40 to $3.50 \text{ m}^{-3} \text{ mm}^{-1}$).
83 Additionally, convective precipitation during Typhoon In-Fa indicated a greater (lower) raindrop concentration than that
84 during Typhoon Taiwan (Hainan), while the raindrop diameter was smaller than those during both Typhoons Taiwan and
85 Hainan. These studies primarily focused on the microphysical process and structure of various weather conditions, which
86 provided insight into the formation process of precipitation.

87

88 At present, there are few studies on the microphysical characteristics of large-scale and global ~~PSsPS~~. On the one hand, as
89 mentioned above, the DSD is influenced by numerous factors, such as precipitation type and season. There may be multiple
90 precipitation types and DSDs in one area. On the other hand, few DSD datasets covering the whole world are available. Dolan
91 et al. (2018) used twelve disdrometer datasets across three latitudinal zones—high-latitude, midlatitude, and low-latitude
92 zones—to analyze DSD spatial variability. They reported that the DSD varies with latitude. At low latitudes, moderate D_m
93 values ($1.5\text{--}2 \text{ mm}$) and large $\log_{10}(N_w)$ values ($> 4 \text{ m}^{-3} \text{ mm}^{-1}$) dominated. At midlatitudes, high D_m values and small N_w

94 values dominated. At high latitudes, low D_m and large N_w values prevailed. The twelve disdrometers mainly located in the
95 United States, Darwin, Finland, and central Indian ocean, and hence Although the dataset covered a wide range of precipitation
96 regimes, it failed to could not capture precipitation microphysical characteristics over all rain climatic regimes. Moreover, a
97 regional DSD dataset cannot represent the DSD within a given latitudinal band because of the limitations of disdrometers.
98 Hence, in this study, GPM DSD products were employed to investigate the microphysical characteristics of ~~PSs~~PS at global
99 scales.

100

101 This study aims to objectively classify PS based on DPR observations using a machine learning approach and to systematically
102 analyze the microphysical characteristics of the resulting PS types. By constructing a unified, data-driven classification
103 framework, the results help clarify regional variability in drop size distributions (DSDs) and provide new insight into the
104 microphysical processes governing different precipitation regimes.~~This study aimed to classify different PSs on the basis of~~
105 ~~DPR observations via machine learning and to analyze the microphysical characteristics of different types of PSs. The results~~
106 ~~could address regional DSD variability and increase our understanding of the microphysical processes of different types of~~
107 ~~PSs.~~ This study is organized in four sections. Section 2 provides detailed descriptions of the GPM data and machine learning
108 models applied in this study. The main results are presented in Section 3, and finally, a summary is given in Section 4.

109 2. Data and methods

110 2.1. Data

111 GPM observations cover the range from 65° S to 65° N (Hou et al., 2014; Tapiador et al., 2012). The GPM DPR operates in
112 the Ka and Ku bands, with a spatial resolution of approximately 5×5 km². The scanning of DPR is cross-track and has three
113 scan patterns: normal scan, matching scan, and high sensitivity scan (Das et al., 2022). Since the scanning pattern of the Ka-
114 band was changed in 2018 (Awaka et al., 2021), the GPM 2A DPR (version 7) products considered the changes in the Ka-
115 band scan pattern with a more accurate precipitation estimation algorithm. The product formats in version 7 have been changed
116 from the original three types to two types: Full scan and High Sensitivity scan. The Full scan product exhibits a new format
117 and is defined as a full-scan dual-frequency product with a 125-m vertical range resolution. Compared with previous algorithms,
118 the FS mode makes it possible for the first time to process a full-scan band of approximately 245 km in dual-band mode
119 (Awaka et al., 2021). Therefore, the observations from the Full scan were adopted in this study.

120

121 In this study, five years (2018–2022) of 2A DPR products (version 7) were employed. The parameters used in this machine
122 learning model ~~are showed in Table 1~~include ~~DSD parameters (D_m and N_w), near-surface precipitation rate (mm h^{-1}),~~
123 ~~attenuation corrected radar reflectivity (dBZ), reflectivity near the surface (Z_{surf}), and typeprecip (stratiform or convective),~~
124 ~~and airTemperature.~~ Detailed descriptions of the generation and retrieval of these parameters can be found in Iguchi et al.
125 (2021). The microphysical variables analyzed here are directly taken from the standard GPM DPR products. Previous studies

126 have extensively evaluated the GPM DPR products on a global scale (Chase et al., 2020; Gatlin et al., 2020; Huang et al., 2022;
 127 Peinó et al., 2024; Seela et al., 2023), supporting their suitability for scientific analyses. It is worth noting that the precipitation
 128 systems analyzed in this study include liquid, mixed phase, and ice phase conditions. The precipitation type helps distinguish
 129 between stratiform and convective precipitation pixels, while air temperature is used to separate snow from rain. To more
 130 strictly exclude potential solid or mixed-phase cases at the surface, this study additionally applies a surface air temperature
 131 threshold (>10 °C) when identifying rain-dominated precipitation systems.

132
 133 **Table1. Summary of the input variables used in the machine learning model, including the original DPR variable names,**
 134 **descriptions, and units.**

<u>Variable name</u>	<u>Long name</u>	<u>Unit</u>
<u>D_m</u>	<u>mass-weighted mean diameter</u>	<u>mm</u>
<u>N_w</u>	<u>normalized intercept parameter</u>	<u>$\text{mm}^{-1} \text{m}^{-3}$</u>
<u>Z_e</u>	<u>reflectivity</u>	<u>dBZ</u>
<u>Zsurf</u>	<u>near-surface reflectivity</u>	<u>dBZ</u>
<u>typeprecip</u>	<u>precipitation type</u> <u>(stratiform/convective)</u>	<u>=</u>
<u>airTemperature</u>	<u>air temperature</u>	<u>K</u>
<u>precipRateNearSurface</u>	<u>near-surface precipitation rate</u>	<u>mm h^{-1}</u>

135

136 **2.2. Precipitation system (PSPS)**

137 This paper presents a method based on the connected domain principle for identifying **PSPS**, similar to those contained in
 138 the widely used TRMM/GPM Precipitation Feature dataset (Liu et al., 2008, 2020). First, pixels with precipitation no less than
 139 0.1 mm h^{-1} are derived from DPR orbit data. Then, neighboring precipitation pixels, including diagonally adjacent precipitation
 140 pixels, are grouped together as a **PSPS**. Each PS is required to have a minimum of four precipitation pixels.

141

142 The DPR provides three-dimensional structure of precipitation and DPR products include radar reflectivity parameters and
 143 retrieved DSD parameters from 0 to 22 km with a range resolution of 125 m. Consequently, for each **PSPS** type, DSD and
 144 radar reflectivity parameters such as the maximum and average values of each layer were calculated. The average D_m and N_w
 145 profiles were used for each PS, and when referring to the maximum D_m and N_w values in each layer, MAX- D_m and MAX- N_w
 146 were used, respectively. The average D_m and N_w profiles were used for each PS, and if the profiles of the maximum D_m and N_w
 147 values in each layer were involved, MAX- D_m and MAX- N_w , respectively, were used. Given the potential relationships of the
 148 convective intensity with microphysical parameters, Z_e in the product was employed to calculate several convection indicators.

149 These include the maximum 20/30/40 dBZ echo top height (MAXHT20/30/40) for each type of PS-PS (Liu, 2011; Liu et al.,
150 2020; Ni et al., 2019; Roy et al., 2020), the echo top height of the PSPS (H_{top}) (Arulraj and Barros, 2021), and other convective
151 parameters. To describe PSPS conditions, several additional features were calculated, including the maximum precipitation
152 rate near the surface (maximum precipitation rate of the precipitation pixels included in the PSPS) and precipitation area (the
153 number of precipitation pixels contained in the PSPS). For the stratiform, convective, land, and oceanic percentages, the
154 corresponding pixel fractions among each individual PSPS were first calculated. These fractions were then averaged across all
155 PSsPS within a given cluster to represent the cluster-level characteristics. Considering that the GPM satellite exhibits a higher
156 observation frequency in high-latitude regions (approximately 2–3 times that at the equator), the original dataset is prone to
157 oversampling in these areas, which can introduce bias. To construct a balanced dataset suitable for clustering analysis, this
158 study implemented a homogenization for the sampling. Specifically, the satellite's observation frequency was calculated as a
159 function of latitude, and sample size for each latitude was adjusted using the ratio of its frequency to that at the equator.
160 Subsequently, precipitation systems were randomly selected from each latitude to ensure a consistent scaled sample size,
161 thereby effectively addressing the issue of uneven sampling. Finally, a total of 8,924,307 PSsPS were obtained for subsequent
162 analysis.

163 2.3. Methods

164 In this study, two distinct machine learning models, namely k-means clustering and principal component analysis (PCA) were
165 used. Both models were trained and evaluated via the Python scikit-learn package. These models are briefly described below.
166 The k-means algorithm is a widely used unsupervised clustering method in machine learning because of its simplicity and
167 computational efficiency (Jain, 2010). The algorithm follows a three-step process. Initially, it aims to select initial cluster
168 centers by randomly obtaining sample coordinates from the dataset and assigning each sample to its nearest cluster center.
169 Next, it computes the mean of all sample points assigned to each previous cluster center to establish new cluster centers. Finally,
170 the algorithm aims to evaluate the differences between the new and old cluster centers. If differences are present, the last two
171 steps are repeated until the cluster centers stabilize and no longer shift (Jain, 2010).

172
173 PCA is a classical dimensionality reduction tool in machine learning (Gang and Bajwa, 2022). PCA is based on the linear
174 combination of target features to construct the principal subspace, and the variance is then employed to measure the information
175 content with the aim of identifying the linear subspace with the maximum variance (Marukatat, 2023). In summary, PCA aims
176 to transform numerous irrelevant features into a comparatively limited number of pertinent ones, thereby retaining as much of
177 the informational content of the original data as possible~~In summary, PCA aims to transform numerous pertinent features into~~
178 ~~a comparatively limited number of irrelevant ones, thereby retaining as much of the informational content of the original data~~
179 ~~as possible~~ (Gang and Bajwa, 2022). In our case, we used PCA to reduce the v dimension, compressing the original 176 height
180 levels into a single representative component for each variable (Ze, Dm, or Nw). Vertically integrated variables (e.g., total
181 water path) are not used here, because while they have clear physical meaning, they aggregate information across the vertical

182 ~~column and may obscure important vertical contrasts relevant to precipitation processes. Only one principal component per~~
183 ~~variable was retained for each profile, as this sufficiently captures the dominant variance of the vertical structure and served~~
184 ~~as a compact descriptor for clustering. Considering that there are 176 vertical layers of GPM DPR products, if all DSD data~~
185 ~~were used as input parameters, the clustering effect could be poor because of the high dimensionality. In this study, PCA was~~
186 ~~adopted to reduce the dimensionality of the data while striking a balance between information loss and the optimal number of~~
187 ~~parameters to be retained (Festa et al., 2023; Jolliffe and Cadima, 2016). The PCA was applied once, independently, for each~~
188 ~~parameter. Time was not treated as an input dimension; only the vertical (height) dimension was reduced. Specifically, PCA~~
189 ~~was independently applied to the vertical profiles of Z_e , D_m , and N_w , each of which originally consists of 176 vertical levels.~~
190 ~~Finally, for each profile of Z_e , D_m , or N_w , the 176 vertical levels are reduced to one single value, which referred to as the first~~
191 ~~principal component score, capturing the dominant variation in the vertical structure.~~

192

193 In this study, all the ~9 million PSsPS derived in section 2.2 are used. Input parameters of each PSsPS for k-means clustering
194 include ~~the maximum precipitation rate near the surface, the echo top height of the PS, the precipitation area~~~~the maximum~~
195 ~~precipitation rate near the surface, H_{top} , the precipitation area~~, the proportion of stratiform precipitation, the proportion of
196 convective precipitation, the DSD parameters (D_m and N_w), the maximum Z_e , and the first principal component score of the
197 vertical profiles of Z_e , D_m , and N_w . These parameters were selected based on their critical role in comprehensively
198 characterizing the features, structure, and microphysical processes of precipitation systems. Among them, the maximum
199 surface precipitation rate and Z_e reflect the intensity of the precipitation process and its echo characteristics, while the
200 precipitation area directly characterizes the spatial differences in ~~both the vertical and~~ horizontal distributions of the system.
201 The H_{top} not only reveals the vertical distribution but also captures the top-level information of the precipitation cloud through
202 the maximum reflectivity height. Introducing the proportions of stratiform and convective precipitation facilitates the
203 differentiation of precipitation types generated by distinct mechanisms, thereby elucidating their evolution patterns and
204 dynamic characteristics. Furthermore, the DSD parameters (D_m and N_w) effectively describe the size distribution of
205 precipitation particles and their intrinsic physical processes, providing an essential basis for an in-depth understanding of
206 precipitation microphysics. ~~Collectively, constructing a multidimensional precipitation feature space with these parameters~~
207 ~~enhances the accuracy and robustness of the clustering analysis.~~

208

209 The quality of clustering was evaluated by analyzing different clustering structures derived from the same dataset. Common
210 clustering performance metrics include the sum of squared errors (SSE), Davis Bouldin (DB) index, Calinski-Harabasz (CH)
211 Score (El Khattabi et al., 2024) and silhouette index, which are widely used to evaluate clustering effectiveness and quality
212 (Ay et al., 2023). In this case, the DB index was calculated by computing the average sum of the intraclass distances between
213 any two clusters divided by the distance between the centers of those two clusters and obtaining the maximum value. The DB
214 index can manage clusters of different sizes and densities with a high degree of robustness to noise and outliers. A lower DB
215 index indicates better clustering performance (Sowan et al., 2023). Additionally, the CH score, which assesses clustering

216 compactness and separation, was also considered. Higher CH scores indicates better-defined clusters. Algorithms with
217 clustering numbers ranging from 3 to 20 were executed, and the resulting change in the DB index and CH score was plotted
218 (refer to Fig. S1 in the Supplementary Material). As shown in Fig. S1, when $K = 8$, the DB index reaches its minimum while
219 the CH index remains at a relatively high level. This indicates that the clustering at $K = 8$ achieves a favorable balance between
220 intra-cluster compactness and inter-cluster separation, supporting the selection of eight clusters as an appropriate classification.
221 Although the CH index reaches its maximum at $K = 11$, the improvement compared with $K = 8$ is marginal. A comprehensive
222 comparison suggests that using 11 clusters would likely introduce unnecessary redundancy without substantially improving
223 clustering performance. Therefore, based on the combined evaluation of multiple clustering validity metrics, this study
224 ultimately classifies the precipitation systems into eight categories.As shown in Figure S1, the DB index reaches its minimum
225 at $K = 8$ and then increases rapidly, whereas the CH score attains its maximum at $K = 11$ with only a slight improvement
226 compared to $K = 8$. Considering the overall trends of both indices, $K = 8$ provides a more balanced and stable clustering
227 structure and was therefore selected as the optimal number of clusters.

228 3. Results and discussion

229 3.1. Global distributions

230 After clustering, each cluster was characterized by its unique precipitation and spatial distribution characteristics, including
231 D_m , MAXHT20/30/40, and convective/stratiform fractions ~~and so on~~. Table 4-2 summarizes the statistics of various parameters
232 for the eight types of PSPS, while Figure 1 illustrates their spatial distributions. For clarity in the subsequent discussion,
233 Clusters 1–8 were grouped and named based on their spatial distributions (Fig. 1) and key precipitation characteristics (Table
234 4-2). Four non-extreme precipitation systems were identified (high-latitude shallow, subtropical shallow, moderate, and deep
235 PSPS), along with four extreme precipitation systems (extreme deep, strong, extreme strong, and marine extreme PSPS).
236 Overall, extreme precipitation systems account for a smaller proportion and exhibit higher MAXHT20/30/40, larger D_m , and
237 stronger precipitation rates compared with non-extreme precipitation systems. Geographically, high-latitude shallow PS are
238 predominantly found poleward of 40°N and 35°S , whereas subtropical shallow PS mainly occur within approximately 20° of
239 the equator. The marine extreme convection type is primarily distributed over oceanic regions. Geographically, high latitude
240 shallow precipitation systems are mainly distributed north of 40°N and south of 35°S , subtropical shallow precipitation systems
241 occur primarily within about 20° on both sides of the equator, and marine extreme convection is mostly located over the ocean.

243 The numbers in Table 4-2 include abundant information and verify the rationality of the objectively clustering algorithm. First,
244 the numbers of the various types of PSPS differed significantly. The two types of shallow PSPS (high-latitude shallow PSPS
245 and subtropical shallow PSPS) accounted for 81.44% of the total PSPS count. The proportions of deep and moderate PSPS
246 were 2.41% and 15.50%, respectively. The other four types of PSPS are regarded as extreme PSPS (extreme deep PSPS, strong
247 PSPS, extreme strong PSPS, and marine extreme PSPS) because they exhibit markedly stronger precipitation intensity (as

248 shown in Figures 4–6) and vertical development than the other categories and occur very infrequently in the global sample,
249 accounting for only 0.39%, 0.22%, 0.02%, and 0.01% of the total PS, respectively because their ratios of the total PS are less
250 than 1%, accounted for only 0.39%, 0.22%, 0.02%, and 0.01%, respectively. In the non-extreme PS_SPS, MAXHT20 is generally
251 positively related to the precipitation rate (Table 4). However, in the extreme PS_SPS, the correlation between the extreme
252 precipitation rate and MAXHT20 is not clear. For example, that the mean value of the maximum precipitation rate in marine
253 extreme PS_SPS was the highest among the eight types of PS_SPS, although its MAXHT20 was less than that in extreme strong
254 PS_SPS and close to that in extreme deep PS_SPS. This result is consistent with other studies noting a weak link between the
255 heaviest rainfall and the highest storm top (Hamada et al., 2015). Although the convective intensity of extreme deep PS_SPS is
256 not significantly higher than that of deep PS_SPS, it exhibits a substantially larger precipitation area and maximum precipitation
257 rate.

258

259 High-latitude shallow PS_SPS was most prevalent at midlatitudes and high latitudes, where snowfall and sleet are more
260 frequent than at low latitudes. Notably, high-latitude shallow PS_SPS were dominated by stratiform precipitation, with stratiform
261 pixels accounting for 88.63%. Meanwhile, approximately 86.60% of the PS_SPS exhibited surface temperatures higher than 0 °C.
262 A study confirmed that at high latitudes and in polar regions, more than 25% of precipitation falls as snow (Lerber et al., 2018).
263 This is consistent with the observations from high-latitude shallow PS_SPS. Additionally, an analysis of high-latitude shallow
264 PS_SPS by latitude revealed that with increasing latitude, the number of samples generally increased. Moreover, the number of
265 PS_SPS with echo top heights less than 2.5 km increased with latitude. During the winter season at 65°S, PS_SPS with echo top
266 heights below 2.5 km accounted for approximately 50% of the total PS_SPS there. This is likely due to the influence of the low
267 surface temperature and weak convection (refer to Fig. S2 in the Supplementary Material).

268

269 Subtropical shallow PS_SPS primarily occurred over the ocean dominated by the subtropical high, with a relatively limited degree
270 of overlap with moderate PS and deep PS (Fig. 1). The mean MAXHT20 value in subtropical shallow PS was only 3.29 km,
271 and the proportion of convective precipitation was the highest among all the types of PS_SPS, exceeding 90%. Compared with
272 those of the other PS_SPS, subtropical shallow PS exhibited the smallest precipitation area. Moreover, it was rarely found over
273 land. These results support the conclusion that subtropical shallow PS is associated with isolated shallow convection over the
274 ocean, which has been the topic of interest in previous studies (Chen and Liu, 2016; Chudler et al., 2022; Houze Jr. et al.,
275 2015).

276

277 The geographic distribution patterns of deep PS and moderate PS were approximately the same (Fig. 1). The number of
278 occurrences in the maritime continent (MC), Indian Ocean, Atlantic Ocean, Amazon rainforests and Pacific Ocean were
279 relatively high. ~~There~~ These regions are generally influenced by the Intertropical Convergence Zone (ITCZ). Nevertheless, the
280 deep PS has higher land percentage. The mean values of the maximum precipitation rates in moderate PS and deep PS were
281 6.21, 35.94 mm h⁻¹, respectively, whereas those of MAXHT20 were 7.03 and 11.89 km, respectively. As a result, the spatial

282 distribution of deep PS is very similar to that of the deep convection core (Ni et al., 2019), which is defined as MAXHT20
283 larger than 10 km.

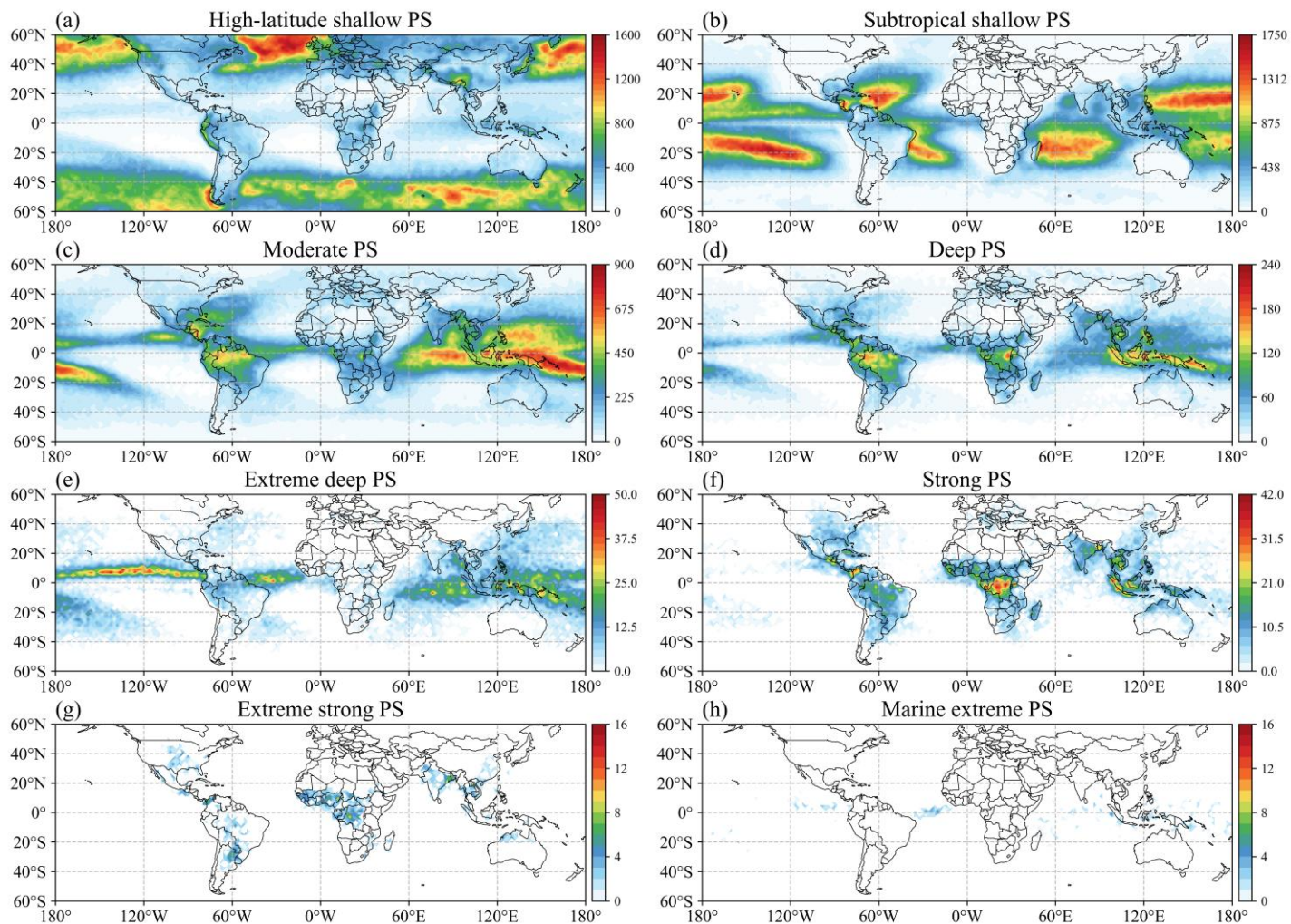
284

285 Strong PS, extreme deep PS, extreme strong PS, and marine extreme PS demonstrated low sample sizes. However, their
286 precipitation areas are significantly larger than non-extreme PS (Table 42). The location of extreme deep PS is similar with
287 moderate and deep PS, with larger values for most parameters. In the extreme strong PS, the proportion of land pixels reaches
288 81%, with significant concentrations in near-equatorial Africa, America, India, the southeastern U.S., and South America. The
289 average maximum precipitation rate in extreme strong PS was 156.37 mm h⁻¹, and MAXHT40 reached 12.32 km, which is the
290 highest among all the types of ~~PSs~~PS. The high MAXHT40 value indicates strong updraft in the middle troposphere, which is
291 a hallmark of intense convection and favors hail formation (Kumar et al., 2023; Zipser et al., 2006). Therefore, the spatial
292 distributions of hailstorms in extreme strong PS were very similar to those of the global hail map derived from spaceborne
293 precipitation radar (Ni et al., 2017) and passive microwave sensor (Bang and Cecil, 2021). Marine extreme ~~PSs~~PS ~~were~~
294 primarily situated in the near-equatorial marine region, with only 943 PS, of which 90% were over the ocean with only 943
295 PSs and 90% is over the ocean. The mean maximum precipitation rate in marine extreme PS was 178.30 mm h⁻¹, ranking first
296 among the eight types of ~~PSs~~PS. Although the MAXHT20 value in marine extreme PS reached 12.81 km, the MAXHT40
297 value in marine extreme PS was approximately half of that in extreme strong PS, indicating low convection activity in the
298 middle and upper levels. This is consistent with the findings of Liu et al. (2007), who observed that the difference between
299 cloud-top height and MAXHT20 over land is smaller than that over the ocean, indicating that convective intensity is stronger
300 over land than over the ocean.

301

302 Oceanic extreme PS (extreme deep PS with a high fraction of ocean pixels and marine extreme PS) have mean precipitation
303 coverage areas exceeding 36000 km², significantly larger than continental extreme PS (strong PS and extreme strong
304 PS)~~Oceanic extreme PS (extreme deep PS and marine extreme PS) with a high fraction of ocean pixels, have mean precipitation~~
305 ~~coverage area exceeding 36000 km², significantly larger than continental extreme PS (strong PS and extreme strong PS).~~ This
306 spatial distribution aligns with previous findings that the most extensive precipitation systems are predominantly located in
307 oceanic regions according to the study of Zhang and Wang (2021). Furthermore, continental extreme PS display markedly
308 stronger convective intensity. This disparity is largely attributable to the observation that the heaviest PS generally occur over
309 tropical land, the Western Pacific warm pool, the North American Great Plains, and Argentina, whereas the most ~~severe-intense~~
310 convective storms are predominantly observed over continental areas (Liu and Zipser, 2015).

311



312

313 **Figure 1.** Spatial distributions ($2^\circ \times 2^\circ$) of the PS counts from 2018 to 2022.

314

315 **Table 12.** Precipitation parameters for the different types of **PSsPS**. (* indicate that in high-latitude shallow PS and
316 subtropical shallow PS, approximately 80% of the samples do not reach 40 dBZ. Therefore, the mean MAXHT40 for these
317 samples is recorded as 0.)

	high- latitude shallow PS	subtropical shallow PS	Moderate PS	deep PS	extreme deep PS	strong PS	extreme strong PS	marine extreme PS
Mean MAXHT20 (km)	3.40	3.29	7.03	11.89	12.67	15.39	17.21	12.85
Mean MAXHT30 (km)	2.63	2.67	5.11	8.65	8.52	13.68	16.31	9.18
Mean MAXHT40 (km)	0.00*	0.00*	3.44	5.53	5.71	8.64	12.32	6.04
Stratiform percentages (%)	88.63	9.46	54.38	53.22	69.90	57.42	53.02	66.83
Convective percentages (%)	5.85	89.95	42.83	44.52	28.16	39.91	44.06	31.56
Land percentages (%)	21.61	6.97	27.96	42.31	15.61	65.37	80.98	10.45
Ocean percentages (%)	78.39	93.03	72.04	57.69	84.39	34.63	19.02	89.55
Mean precipitation (mm h ⁻¹)	1.60	2.35	6.21	35.94	156.67	135.46	156.37	178.30
precipitation Standard deviation (mm h ⁻¹)	1.63	1.92	8.89	50.44	98.44	106.95	103.50	98.61
Number of samples	4,184,547	3,083,077	1,383,261	215,611	34,982	19,790	2,096	943
Mean precipitation area (km ²)	610.57	239.23	2761.46	7009.37	37076.93	18485.91	22521.51	36044.11
>273.15 K frequency (%)	86.60	99.16	99.83	99.97	99.97	99.99	99.99	100.00
2.5 km Mean MAX-log10(N _w) [m ⁻³ mm ⁻¹]	3.47	3.70	4.06	4.49	5.20	4.72	4.88	6.07
2.5 km Mean MAX-D _m [mm]	1.03	1.17	2.26	2.82	2.71	3.04	3.11	2.61
2.5 km Mean log10(N _w) [m ⁻³ mm ⁻¹]	3.23	3.45	3.36	3.39	3.83	3.36	3.35	4.45
2.5 km Mean D _m [mm]	0.85	0.89	1.36	1.50	1.30	1.61	1.71	1.32

318 3.2. Global distributions of microphysical features

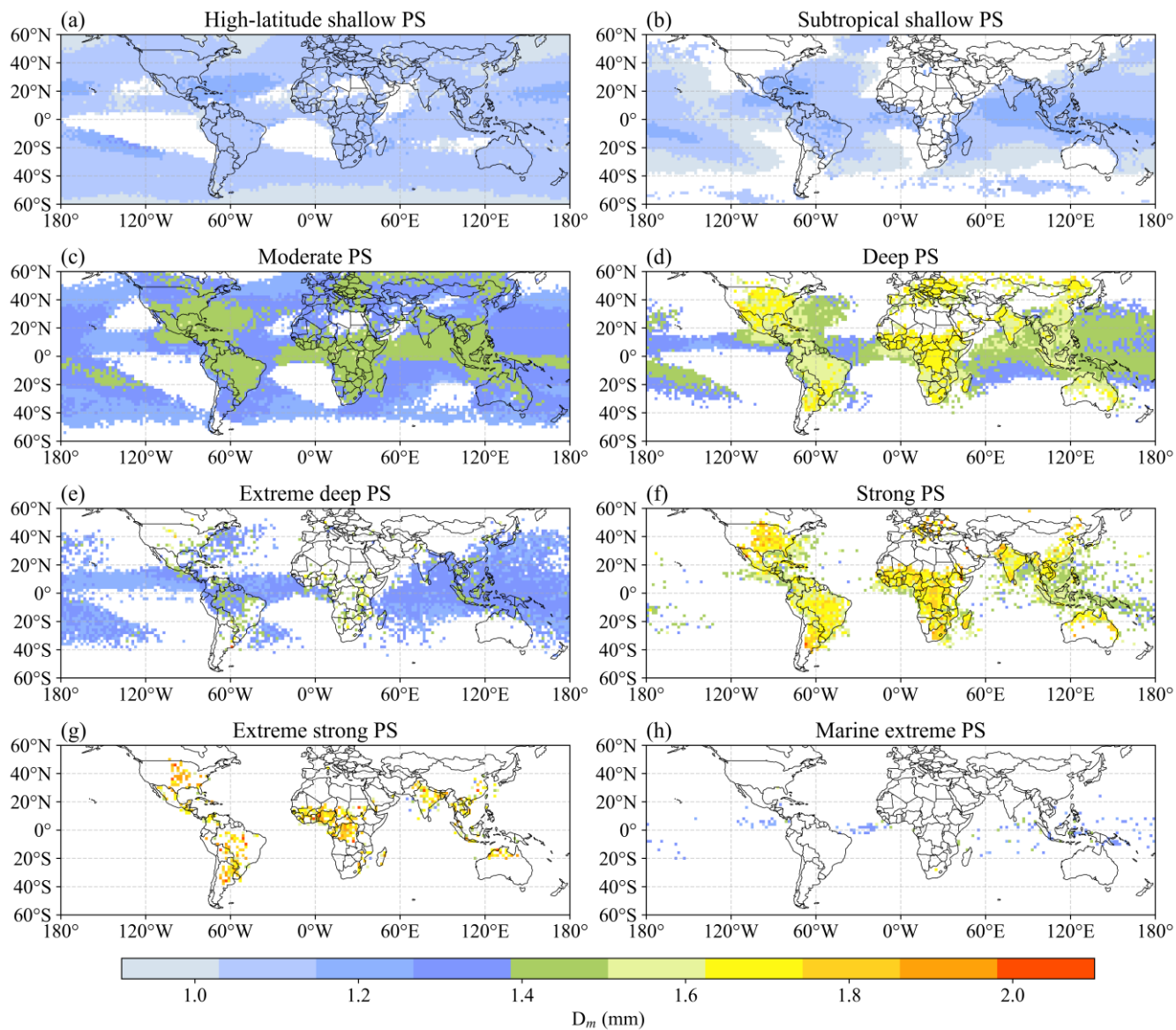
319 Fig. 2 and Fig. 3 show the global distributions of the microphysical parameters for the eight types of **PSsPS**. To avoid the
320 influence of ground clutter, in each PS, the mean D_m and N_w values at 2.5 km above the ground surface were analyzed. Notably,

321 there was a significant degree of spatial heterogeneity in each panel. The general conclusion is that continental **PSsPS** exhibit
322 a higher D_m than do oceanic **PSsPS**. Usually, continental rainfall is associated with high convective activity in which clouds
323 produce large raindrops. In contrast, oceanic rainfall is accompanied by the formation of weak updrafts and the development
324 of a low melting layer, which impedes the formation of large raindrops and results in a high concentration of small raindrops
325 (Saha et al., 2022; Seela et al., 2018). Moreover, D_m decreases with increasing latitude, a trend that is especially notable in
326 high-latitude marine regions (refer to Fig. S2c in the Supplementary Material). Cha et al. (2021) noted that snow primarily
327 comprises small particles (diameter < 1 mm). In high-latitude shallow PS, snowfall may become more frequent from the middle
328 to high latitudes, which can result in a decrease in D_m . Notably, the height and thickness of the melting layer may influence
329 raindrop growth (Hu et al., 2024). With increasing latitude, the melting layer becomes thinner, thus reducing the conditions
330 necessary for raindrop growth, which may lead to the formation of a larger number of small raindrops. In the oceanic regions
331 within subtropical shallow PS, the higher sea surface temperature in the tropics is more conducive to convection formation
332 and development. Moreover, D_m varies among the eight clusters in a specific region. For example, in the Amazon region,
333 moderate PS exhibits a lower D_m than deep PS does.

334

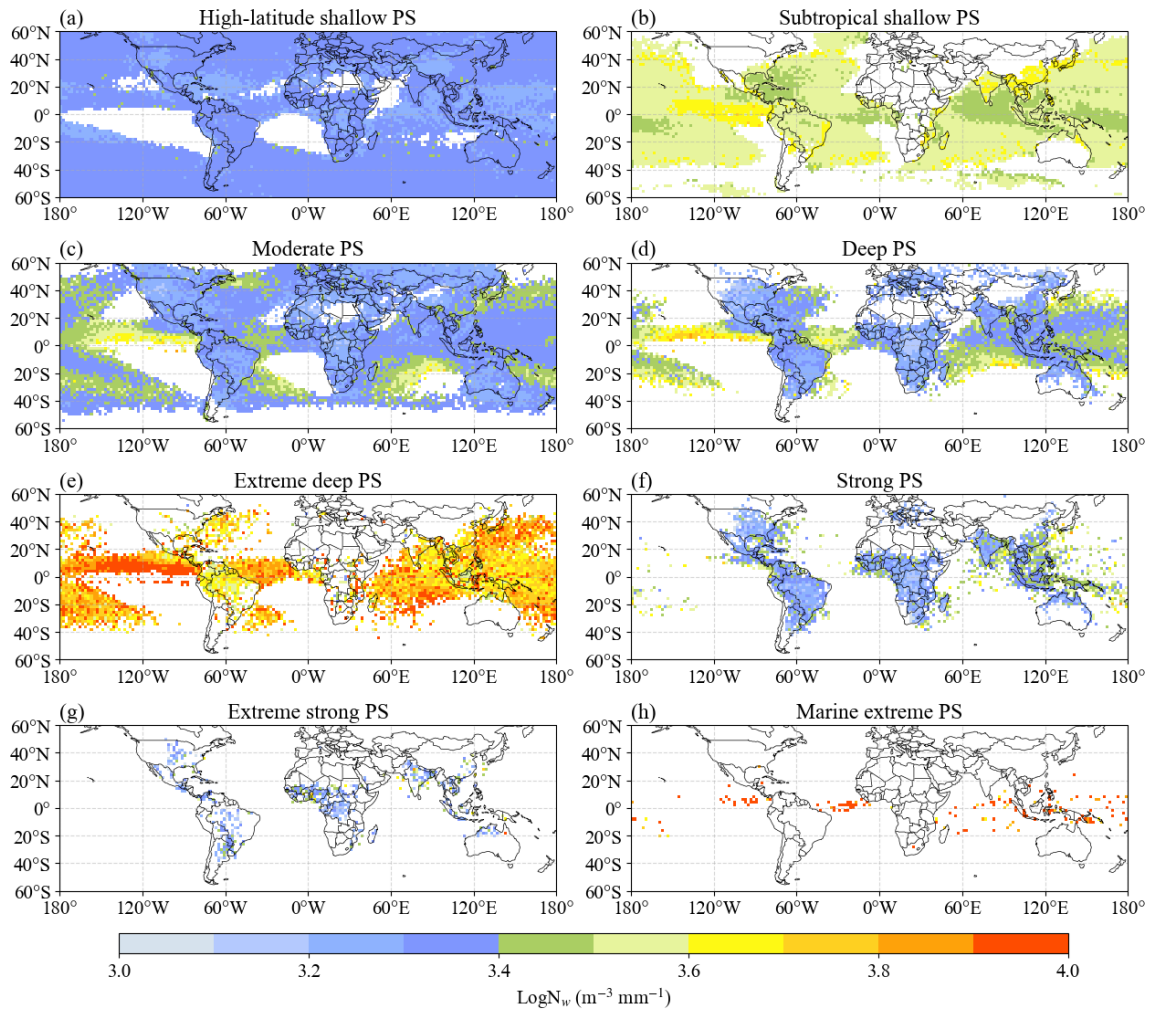
335 Similar to D_m , there is a distinct contrast in N_w between continents and oceans (Das and Chatterjee, 2018). Continental rainfall
336 is usually associated with the cold rain mechanism, whereby raindrops grow as ice particles (Gupta et al., 2023). In contrast,
337 oceanic rainfall is associated with a warm rain regime, in which raindrops grow via a collision-agglomeration mechanism.
338 Consequently, N_w over land is less than that over oceans (Suh et al., 2016). For the same PS, N_w is high in areas with small D_m
339 values and conversely low in areas with large D_m values. For example, in extreme deep PS, the D_m value over the eastern near-
340 equatorial Pacific Ocean, which reaches approximately 1.18 mm, is smaller than that of the other oceanic regions. However,
341 N_w is significantly greater than those in the other regions. In strong PS, the D_m values in near-equatorial Africa and the eastern
342 United States are greater than those in other regions, but the N_w values are lower than those in other regions. It is possible that
343 D_m and N_w may be negatively correlated for the same PS.

344



345

346 **Figure 2.** Spatial distributions of the mass-weighted mean diameter (D_m) for the eight PS clusters at a height of 2.5 km.



347

348 **Figure 3.** Similar to Fig. 2. but for $\text{log}_{10}(N_w)$.

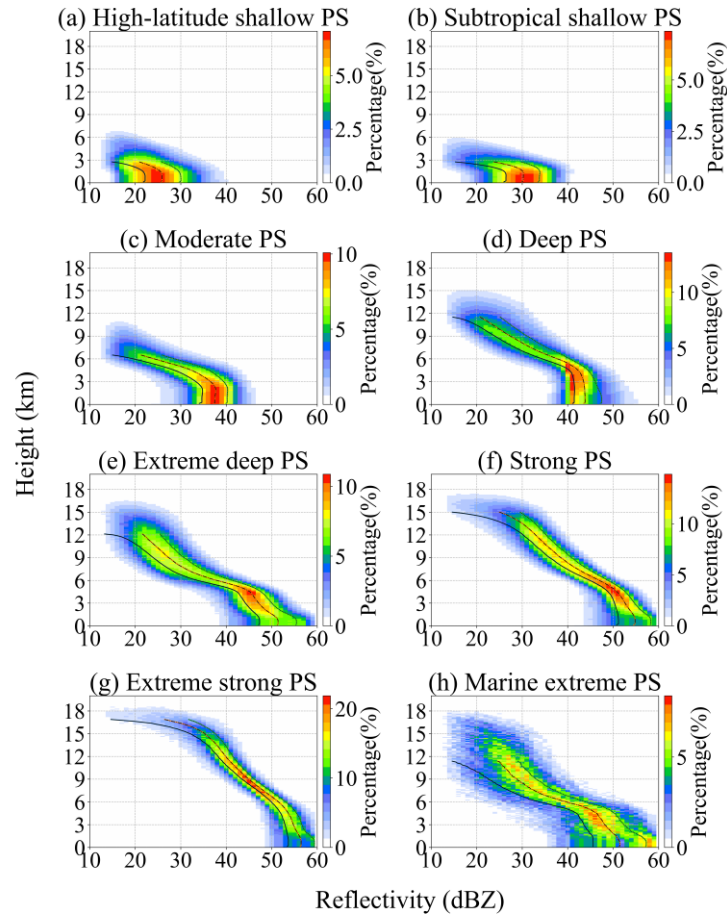
349 3.3. Vertical structure of the different PS types

350 The contoured frequency by altitude diagrams (CFADs) of D_m , N_w , and the maximum radar reflectivity for the eight clusters
 351 are shown in Fig. 4/5/6. Figure 4 shows the CFAD of the maximum radar reflectivity profiles. The results revealed high echo
 352 tops for deep PS, extreme deep PS, strong PS, and extreme strong PS, and low echo tops for high-latitude shallow PS and
 353 subtropical shallow PS. Extreme strong PS attained an echo top height greater than 18 km, and it also exhibited the strongest
 354 convection at the middle level. Its geographic distribution was exclusively terrestrial, which is consistent with other studies
 355 concluding that deep convective cores occur mostly over land (Houze Jr. et al., 2015). Extreme deep PS and marine extreme
 356 PS exhibited sharper decreasing trends from 6–12 km than extreme strong PS, indicating weaker convective updrafts. In
 357 contrast, extreme strong PS had stronger updrafts, producing more supercooled liquid droplets and large ice–water vapor

358 condensates (Jiang, 2012). In contrast, extreme deep PS and marine extreme PS showed lower 40 dBZ echo tops and a more
359 rapid decrease in reflectivity above the freezing level. This suggests relatively weaker mid- and upper-level updrafts, which
360 limit the vertical transport of ice particles and reduce the abundance of supercooled liquid and large condensate.

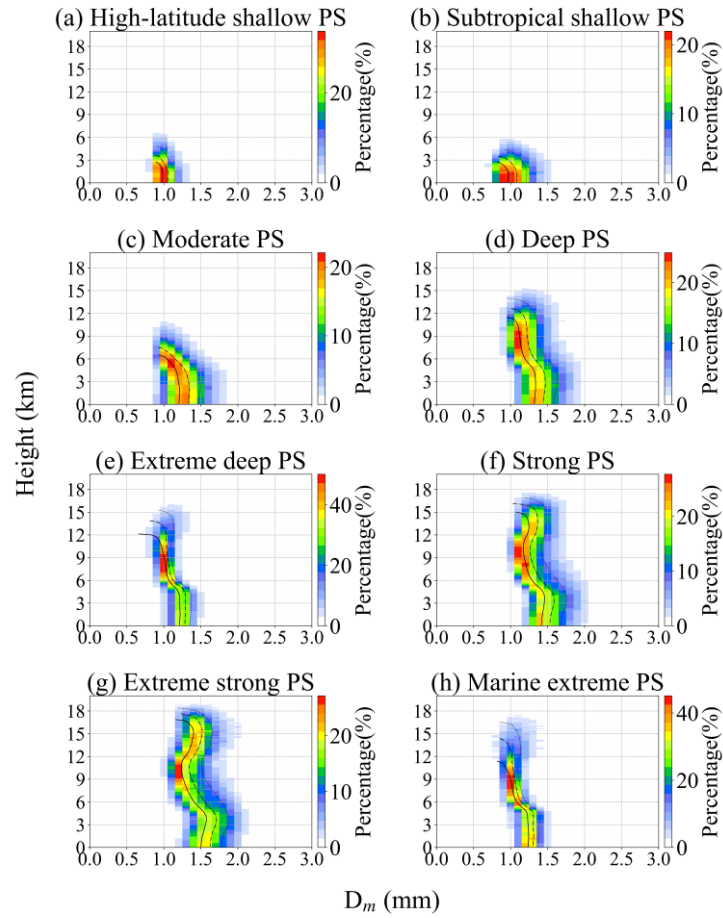
361

362 Table 4-2 indicates that the land proportion of extreme strong PS was much greater than that of extreme deep PS and marine
363 extreme PS. Additionally, compared with oceanic environments, land regions are generally characterized by relatively
364 drier conditions and lapse rates closer to the dry adiabatic profile, which enhance buoyancy and allow stronger updrafts to loft
365 ice crystals to higher altitudes, indicates a dry adiabatic lapse rate, which results in greater buoyancy and allows for stronger
366 updrafts to lift ice crystals higher into the atmosphere. As a result, the maximum radar reflectivity in the middle levels at high
367 altitudes decreased more slowly in extreme strong PS. High-latitude shallow PS and subtropical shallow PS yielded low echo
368 tops of less than 6 km, indicating low convective intensity. Therefore, subtropical shallow PS could be identified as being
369 associated with isolated shallow convection over the ocean, especially the region dominated by the subtropical high.



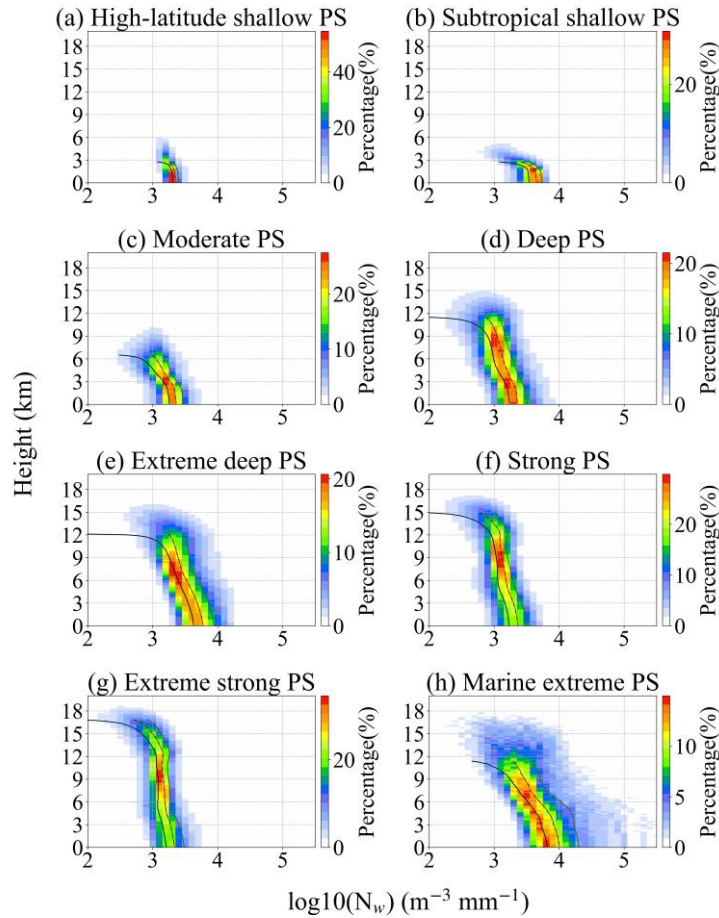
370

371 **Figure 4.** Contoured frequency by altitude diagrams (CFADs) of the maximum radar reflectivity for the eight distinct PS
 372 clusters. The solid lines indicate the 25th percentiles; the dashed-dotted lines indicate the 50th percentiles; the dotted lines
 373 indicate the 75th percentiles.



374

375 **Figure. 5.** Similar to Fig. 4, but for D_m .



376

377 **Figure 6.** Similar to Fig. 4, but for $\log_{10}(N_w)$.

378 Figure 5 shows the CFAD of D_m for the eight types of **PSs**. Generally, deep convections (deep PS, extreme deep PS, strong
 379 PS, extreme strong PS, and marine extreme PS) produce different D_m values in the regions above and below approximately 5
 380 km. Moreover, strong PS and extreme strong PS exhibited wider distributions than those of extreme deep PS and marine
 381 extreme PS. For deep PS, strong PS, and extreme strong PS, D_m below 4.8 km did not change much or slightly increased along
 382 with height, but the value decreased between 4.8 and 6.9 km. In extreme strong PS, the vertical structure of D_m was more
 383 complex. Extreme strong PS exhibited three regimes according to the variations in D_m . The first regime was observed between
 384 0 and 4.1 km, where D_m increases with altitude. This is consistent with other papers involving the use of ground-based radar
 385 observations and reporting that D_m of deep convective precipitation decreases with decreasing height near the surface (Marzuki
 386 et al., 2023). The observed decrease in D_m may be related to the continued breakdown of large isolated raindrops in the

387 atmosphere. The second regime was observed above the freezing level, from 4.1 to 10 km, where D_m decreases with altitude.
388 In this regime, the updraft in deep convection was decreased (Uma and Rao, 2009). The decline in updraft decreased the size
389 of the particles that can be retained in the cloud. The rapid changes of D_m between the two regimes might be due to the changes
390 of precipitation phase across the melting layer. As revealed by Mroz et al. (2024), the routinely retrieval algorithm results in
391 rapid changes of D_m and mass flux around the melting level, because the DPR observations cannot quantify ice water content
392 and ice crystal size above the stratiform rain regions~~the DPR observations cannot quantify ice particle content and their size~~
393 ~~above the stratiform rain regions~~. Finally, the third regime was observed between 10 and 18 km, where D_m increases with
394 altitude and where strengthened updrafts are often observed (Becker and Hohenegger, 2021). Although both high-latitude
395 shallow PS and subtropical shallow PS were shallow PSsPS, subtropical shallow PS had a wider distribution of D_m than high-
396 latitude shallow PS. One possible reason is that in shallow oceanic convection, the breaking of large raindrops broadens the
397 DSD.

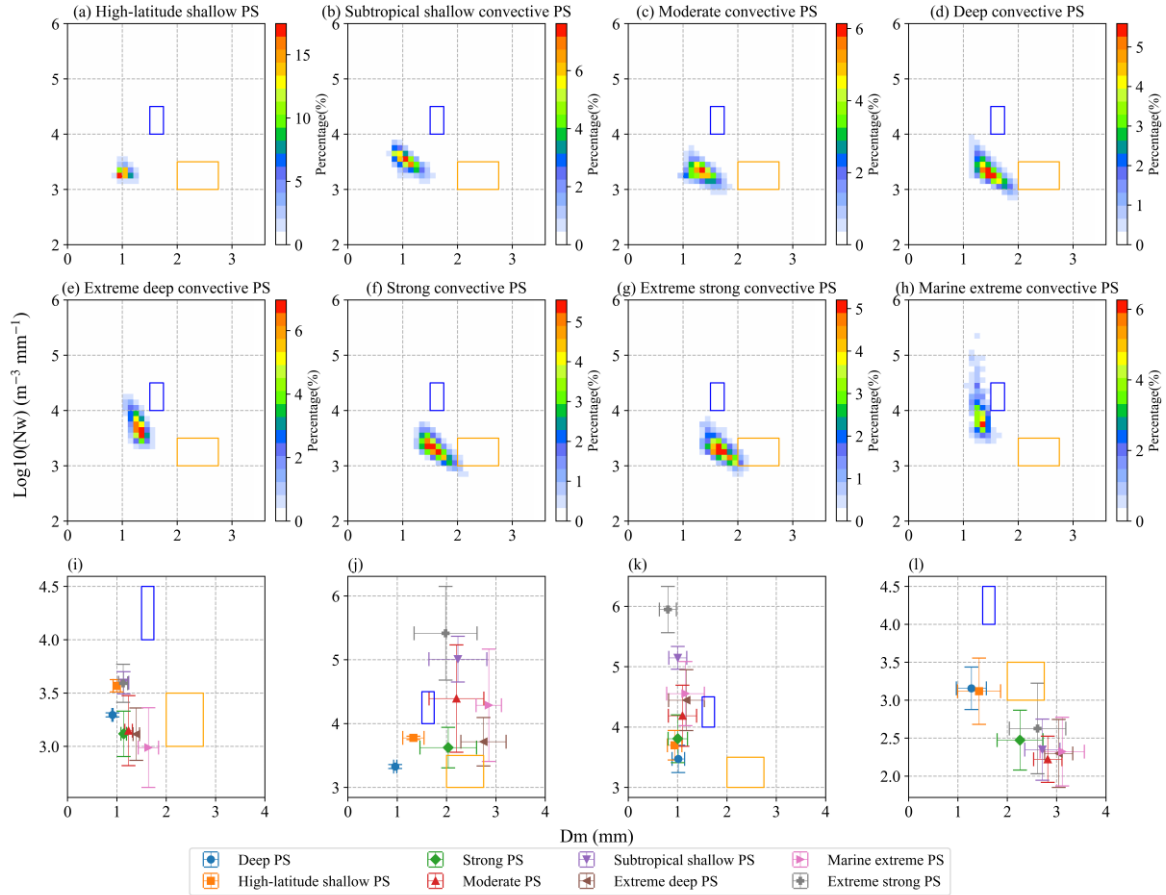
398

399 Figure 6 shows the CFAD of $\log_{10}(N_w)$ for the different types of PSsPS. In general, N_w decreases with increasing altitude.
400 The distribution range of N_w for shallow PSsPS was relatively small. Moreover, the N_w distribution range of subtropical
401 shallow PS was larger than that of high-latitude shallow PS. Among PSsPS with intense convection, PS with a greater
402 proportion of land coverage exhibited a narrower distribution of N_w ~~PSs with a greater proportion of land coverage exhibited~~
403 ~~more concentrated N_w values~~, whereas PSsPS with a greater proportion of ocean coverage exhibited higher N_w values. For
404 example, the N_w values of strong PS and extreme strong PS were smaller and narrower than those of ocean-dominated deep
405 PS, extreme deep PS and marine extreme PS. This finding is consistent with the conclusions of other studies (Kumar et al.,
406 2024). One possible explanation is that the slower updrafts over ocean regions result in higher concentrations of smaller
407 condensates at lower altitudes. Moreover, for both D_m and N_w , the four non-extreme PSsPS exhibit little vertical variation
408 below the melting layer, which may be attributed to a balance between coalescence and breakup processes.

409 **3.4. DSD characteristics at a height of 2.5 km**

410 Figure 7a-h show the frequency distributions of the mean D_m and $\log_{10}(N_w)$ values observed at 2.5 km above ground level.
411 The mean D_m values and the corresponding $\log_{10}(N_w)$ values for the eight types of PSsPS are detailed in Table 4.2. Generally,
412 all the distributions shown in Fig. 7a-h greatly deviate from the parameters of continental convection and maritime convection
413 defined by Bringi et al. (2003). One reason is that the mean values of D_m and N_w for one PS were considered here, whereas
414 Bringi et al. (2003) separated the observation samples into stratiform and convection-convective samples. Moreover, the DSDs
415 observed by disdrometers are generally cumulative observations of a single storm at one fixed location and differ from the
416 results for each PS in this study, which represent the instantaneous occurrence of a storm. With the most intense convection at
417 the middle level, extreme strong PS was the closest to continental convection (Fig. 7d), whereas marine extreme PS was the
418 closest to maritime convection (Fig. 7e). For most PSsPS, D_m and N_w were negatively correlated, with greater dispersion of
419 D_m than that of N_w . However, it should be noted that the observed correlations between D_m and N_w may partly be due to the

420 retrieval assumptions in the GPM algorithm, which enforces a correlation between D_m and precipitation rate (Chase et al.,
 421 2020), rather than purely physical relationships. Moreover, the shallow PSsPS exhibited lower D_m and N_w values and
 422 narrower~~more concentrated~~ distributions than those of the deep PSsPS.



423
 424 **Figure 7.** (a-h) Two-dimensional frequency distributions of D_m and $\log_{10}(N_w)$ at a height of 2.5 km, and (i-l) statistical values
 425 of $\log_{10}(N_w)$ and D_m for each PS (the bar indicates one standard deviation). (i) Mean values of D_m and $\log_{10}(N_w)$, (j) MAX-
 426 D_m and MAX- $\log_{10}(N_w)$, (k) MAX- $\log_{10}(N_w)$ and D_m at its corresponding position, and (l) MAX- D_m and $\log_{10}(N_w)$ at its
 427 corresponding position for each PS. (The blue and orange rectangles denote the maritime and continental convective clusters,
 428 respectively, in D_m and $\log_{10}(N_w)$ space from Bringi et al. (2003)).

429
 430 To further compare the mean D_m and N_w values of the different clusters, Figure 7i shows a summary of the mean D_m and N_w
 431 values, with the standard deviation for each type of PS. Marine extreme PS showed a significant abnormal low value of N_w ,
 432 whereas the N_w value of extreme deep PS slightly deviated from those of the other PS. If only the three extreme deep PSsPS

433 with the highest echo tops (strong, extreme strong, and marine extreme PS) are considered, D_m and N_w show an inverse
434 relationship. These results might suggest that in deep convection, the DSD parameters at the near-surface level are related to
435 convection intensity parameters. Ni et al. (2019) revealed that the dual-frequency ratio between the Ku and Ka bands at 12
436 km was positively correlated with intensity parameters such as MAXHT20/30, partly because stronger updrafts could hold
437 larger ice particles in clouds.

438

439 Note that ~~although~~ the mean D_m and N_w values do not capture the variety of DSDs in each PS. For example, the DSD might
440 differ between convective and stratiform regions, where the N_w - D_m relationships might vary. To comprehensively demonstrate
441 the microphysical features of PSsPS, Figure 7j shows the mean MAX- D_m and MAX- N_w values of each PS at 2.5 km. For
442 extreme PS, MAX- D_m and MAX- N_w were negatively correlated, while a positive correlation was observed for non-extreme
443 PS. A similar relationship is also shown in Fig. 7k, which suggests a relationship between MAX- N_w and the corresponding D_m
444 value in the MAX- N_w pixels of each PS. Nevertheless, as shown in Fig. 7k, the D_m values of all eight types of PSsPS were
445 very close. Nevertheless, it could be also found that in the non-extreme PS the D_m increases with MAX- N_w , while in the
446 extreme PS, the D_m decreases with MAX- N_w . Figure 7l shows the relationship between MAX- D_m and the corresponding N_w
447 value in the MAX- D_m pixels of each PS. Interestingly, for all eight types of PSsPS, MAX- D_m and N_w showed significantly
448 negative correlations. Note that MAX- D_m and MAX- N_w in Fig. 7j are the maximum values for one PS and usually do not occur
449 in the same pixel. Figure 7k-l show the N_w - D_m relationship observed at the same location. Overall, the conclusions generally
450 indicated that deep PSsPS yield larger MAX- N_w or MAX- D_m values than shallow convection PSsPS do. Overall, extreme PS
451 exhibited negative correlations between N_w and D_m , whereas non-extreme PS demonstrated positive correlations.

452

453 ~~Ryu et al. (2021) analyzed DSDs during three types of heavy rainfall events with different rain intensities. They also reported~~
454 ~~that D_m increases with increasing rainfall intensity, whereas N_w decreases with increasing rainfall intensity.~~ In this study, we
455 saw a positive relationship between the increase in D_m and MAXHT20 in extreme PS. However, extreme strong PS attained
456 the highest MAXHT20 value, but its precipitation rate was lower than that of extreme deep PS and marine extreme PS. These
457 results suggest a complex relationship between the microphysical parameters and convection features, especially in deep and
458 intense convection systems. Notably, in extreme convection, intense precipitation at lower storm levels can cause significant
459 rain-induced attenuation of the radar signal, which may in turn influence the retrieval accuracy of microphysical
460 parameters. ~~Notably, in extreme convection, with strong convection at the top of the storm, attenuation becomes notable at low~~
461 ~~storm levels, which might influence the retrieval of microphysical parameters.~~ To assess the impact of attenuation on the D_m -
462 N_w relationship, ground-based observations of microphysical properties from disdrometers are needed. Finally, we considered
463 the PS as a whole. The microphysical characteristics varied among different pixels. The mean or maximum values of D_m and
464 N_w only reflect part of the total process. Therefore, analyses on the basis of pixel-level observations would improve this work.

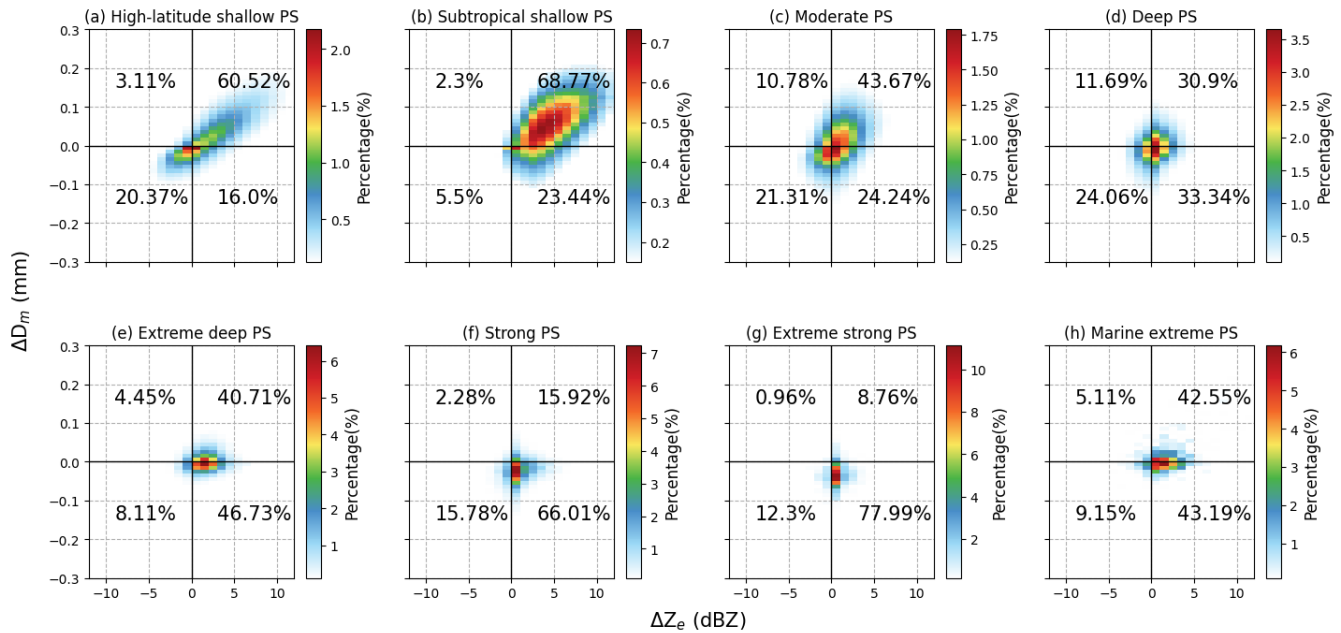
465

466 To gain further insight into the primary microphysical processes associated with the various PS, we employed an investigative
467 approach analogous to that utilized by Kumjian and Prat (2014). To prevent the influence of ground-based clutter, ΔZ_c and
468 ΔD_m values were calculated as the difference between Z_c and D_m at 2 and 3 km above the ground. Specifically, $\Delta Z_c = Z_c^{2\text{km}} -$
469 $Z_c^{3\text{km}}$ and $\Delta D_m = D_m^{2\text{km}} - D_m^{3\text{km}}$ are calculated. Fig. 8 shows the frequency pattern of ΔZ_c versus ΔD_m for the eight types of
470 ~~PSs~~PS. An increase (decrease) in Z_c and D_m indicates that coalescence (breakup) processes dominate. Balanced breakup and
471 coalescence processes result in an increase in Z_c but a decrease in D_m . In contrast, a decrease in Z_c and an increase in D_m are
472 due to ~~predominantly predominate~~ evaporation or size sorting processes (Wen et al., 2023).

473

474 The microphysical processes of the different types of ~~PSs~~PS ~~were significantly distinct~~ exhibited clear differences. Notably,
475 the microphysical processes were dominated by coalescence in the two types of shallow PS (Fig. 8a-b). Previous studies have
476 demonstrated that high-latitude shallow PS are more likely to experience the condensation of rain droplets into snow due to
477 the low temperatures in these regions (Thompson et al., 2015). Meanwhile, the coalescence process plays an important role in
478 tropical oceanic shallow convective precipitation (subtropical shallow PS) as demonstrated by Li et al. (2024). Balanced
479 breakup and coalescence processes in extreme PS accounted for more than 40% of the total microphysical processes,
480 significantly exceeding the other three types of microphysical processes~~Balanced breakup and coalescence processes in the~~
481 ~~microphysical processes of extreme PS accounted for more than 40% of the total microphysical processes, significantly~~
482 ~~exceeding other three types of microphysical processes~~. The microphysical processes may reach an equilibrium state under
483 high rainfall rates, in which the coalescence and breakup of raindrops are nearly balanced. These results are consistent with
484 Shi et al. (2025), who found that extreme rainfall is primarily driven by vigorous mixed-phase processes and a balance between
485 coalescence and breakup in liquid-phase processes. Extreme deep PS and marine extreme PS encompassed a higher percentage
486 of coalescence processes than strong PS and extreme strong PS did, whereas strong PS and extreme strong PS encompassed a
487 higher percentage of breakup processes.

488



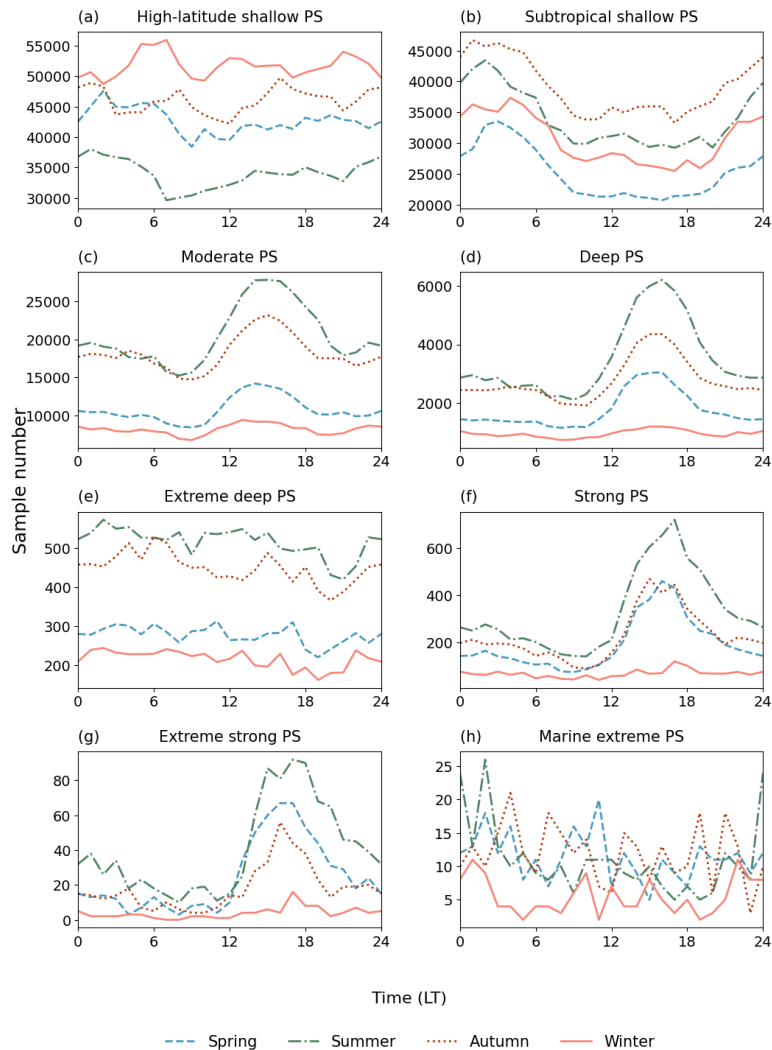
489

490 **Figure 8.** Frequency pattern of ΔZ_e versus ΔD_m between 2 and 3 km for the eight PS clusters.

491 3.5. Seasonal and diurnal cycles

492 In this study, seasons were categorized by fixed calendar months. The Northern Hemisphere seasons were defined as spring
 493 (March–May), summer (June–August), autumn (September–November), and winter (December–February). Conversely, the
 494 Southern Hemisphere seasons followed the opposite pattern: spring (September–November), summer (December–February),
 495 autumn (March–May), and winter (June–August). Based on this classification, the subsequent analysis examines seasonal and
 496 diurnal variations in PS frequency and microphysical parameters. Figure 9 shows the cycles of PS occurrence. Overall, the
 497 seasonal and diurnal cycles differed among the eight types of PSs. Moderate PS, deep PS, strong PS, and extreme strong
 498 PS exhibited cycles like those of continental convection systems, with peaks in the afternoon and in summer. Dominated by
 499 tropical shallow convection over the ocean (Fig. 1), subtropical shallow PS occurred mostly between 00:00 and 05:00 local
 500 time and was more frequent during the autumn season than during the other seasons, with the lowest occurrence
 501 during the spring season. The other types of PS (high-latitude shallow PS, extreme deep PS, and marine extreme PS) did not
 502 show obvious diurnal cycles, except that high-latitude shallow PS indicated a low peak at approximately 6 am in winter and a
 503 valley before noon in summer. High-latitude shallow PS occurred infrequently in winter. Extreme deep PS occurred more
 504 frequently in summer and autumn, with fewer occurrences in winter. Note that marine extreme PS did not demonstrate obvious
 505 seasonal discrepancies, but ~~shown~~ showed a peak at night in the summer. Specifically, strong PS and extreme strong PS with
 506 a higher proportion over land exhibit a peak occurrence around 3 p.m. in the afternoon. In contrast, extreme deep PS and
 507 marine extreme PS mostly show no distinct peak, with frequencies distributed evenly throughout the day. This difference

508 reflects the land-ocean contrast in extreme PS, which is consistent with findings from other related studies (Wang and Tang,
 509 2020).
 510

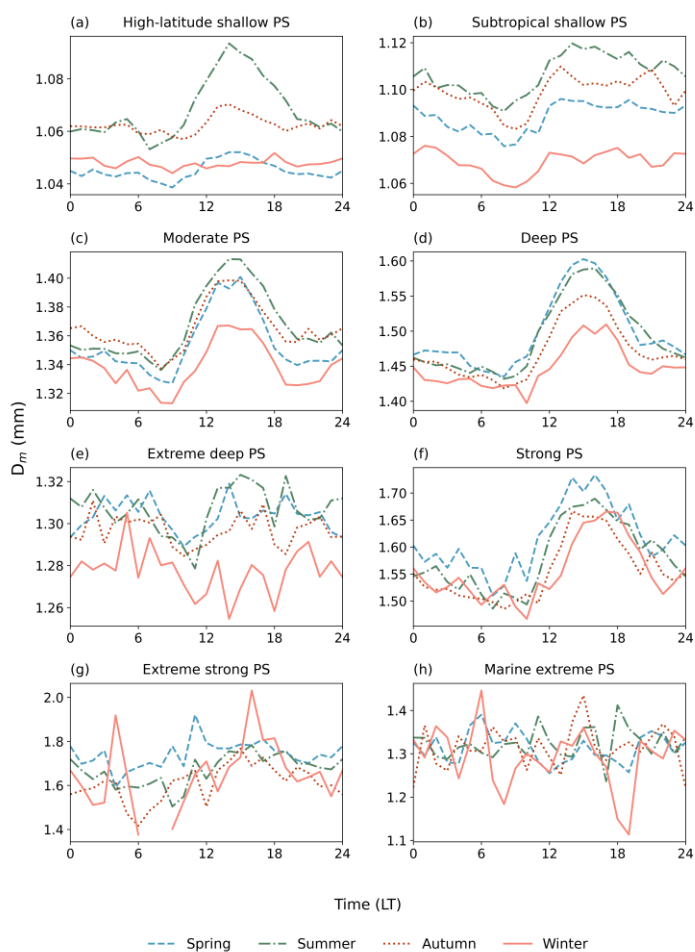


511

512 **Figure 9.** Diurnal variations in the sample sizes of the eight distinct PS clusters across the four seasons.

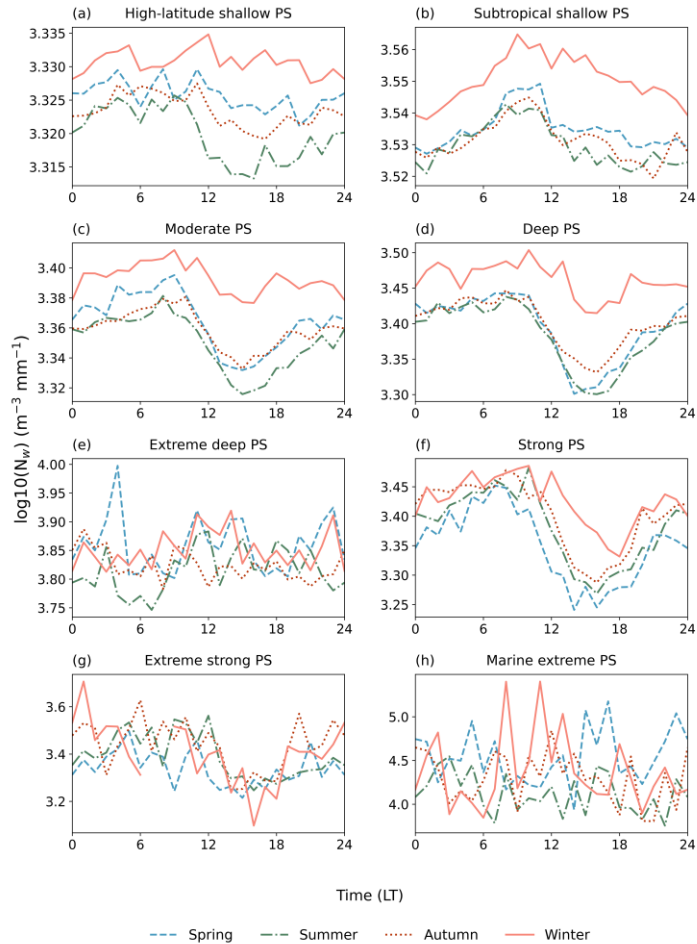
513 Figures 10 and 11 show the seasonal and diurnal cycles of D_m and N_w , respectively. The diurnal cycles of D_m were similar
 514 with those of PS occurrence to some extent. For example, in moderate PS, deep PS and strong PS, both the occurrence and D_m
 515 have peaks ~~in the~~ around 15 pm. One connection between these two parameters is that environments that favor storm
 516 occurrence could also facilitate the development of stronger updrafts, which could promote the formation of large particles in
 517 clouds. Nevertheless, discrepancies are obvious between the cycles of occurrence and D_m . For example, the D_m in the extreme
 518 strong PS did not show obvious diurnal variations. The high-latitude shallow PS shows a peak in the summer (Fig. 10a), which

519 is not found in the diurnal cycle of occurrence (Fig. 9a). In subtropical shallow PS, the diurnal cycle of D_m (Fig. 10b) was the
 520 opposite to that of PS occurrence (Fig. 9b). The diurnal variation of N_w differed substantially from that of D_m and occurrence
 521 frequency. The diurnal cycles of N_w were basically different with those of D_m and occurrence. In subtropical shallow PS,
 522 moderate PS, deep PS, and strong PS, the N_w peaked in the morning. Nevertheless, the diurnal cycles of subtropical shallow
 523 PS, moderate PS, and deep PS also differed. For example, N_w of subtropical shallow PS at night was low, whereas N_w of
 524 shallow convective PS and moderate PS at night was very close to its peak. Extreme deep PS and marine extreme PS did not
 525 exhibit obvious diurnal cycles of N_w . The extreme strong PS showed low values of N_w in the afternoon and little variations
 526 at night. For high-latitude shallow PS, diurnal variation is not clear except in the summer when the N_w in the afternoon is the
 527 lowest.



528

529 **Figure 10.** Similar to Fig. 9 but for mean D_m value.



530

531 **Figure 11.** Similar to Fig. 9 but for the mean $\log_{10}(N_w)$ value.

532 Similar to the diurnal cycles, the annual cycles of D_m and N_w were opposite in subtropical shallow PS, moderate PS, and deep
 533 PS, of which D_m was the lowest and N_w was the largest in winter. Nevertheless, there were also differences in the annual cycles
 534 of the three types of PSs. For example, in subtropical shallow PS, D_m was the largest in summer, followed by autumn and
 535 spring, whereas the N_w values during the three seasons were very close. Among the extreme PS, N_w and D_m did not exhibit
 536 obvious annual cycles. For high-latitude shallow PS, the highest D_m value occurs in summer and the D_m in winter and spring
 537 were comparable. However, the annual cycle of N_w attained the largest value in winter and the lowest value in summer.

538 4. Conclusions

539 In this study, GPM DPR data were used to objectively classify global PS and analyze the microphysical characteristics of the
540 different types of PS. The main conclusions are as follows:

541

542 1). By conducting an objective classification of global ~~PSs~~PS via key parameters such as the convective intensity, radar
543 reflectivity, and DSD parameters, eight distinct types of ~~PSs~~PS were identified. These systems were classified on the basis of
544 their unique microphysical and ~~convection-convective~~ properties, providing a detailed understanding of the different
545 precipitation processes worldwide. The eight types of ~~PSs~~PS identified are as four types of regular/non-extreme PS (high-
546 latitude shallow PS, subtropical shallow PS, moderate PS, deep PS) and four types of extreme PS (extreme deep PS, strong
547 PS, extreme strong PS, marine extreme PS).

548

549 2). MAXHT20 is generally correlated with the precipitation rate, but this relationship is not clear for extreme PS. The
550 relationship between MAXHT20 and D_m does not follow a simple linear pattern. For extreme PS, MAXHT20 is positively
551 related to D_m at 2.5 km above the ground surface. This may reflect the relationship between higher cloud tops and greater
552 liquid water contents in strongly convective ~~PSs~~PS. However, for non-extreme PS, the relationship between MAXHT20 and
553 D_m is more complex and may be influenced by variations in the physical processes of the different PS.

554

555 3). For the same type of PS, D_m over land is greater than that over the ocean. Additionally, D_m exhibits latitudinal variability,
556 particularly in high-latitude shallow PS, where D_m decreases with increasing latitude. Additionally, continental rainfall is often
557 associated with lower N_w values due to the dominance of the cold-rain (ice-phase) process, in which precipitation particles
558 grow through riming and aggregation above the freezing level, typically producing larger but fewer drops after melting.~~is~~
559 ~~associated with lower N_w values due to the cold-rain mechanism; In contrast, oceanic rainfall is more frequently governed by~~
560 ~~the warm-rain process dominated by collision-coalescence below the freezing level, which tends to generate more numerous~~
561 ~~but smaller raindrops and thus higher N_w values, whereas oceanic rainfall is associated with higher N_w values resulting from a~~
562 ~~warm-rain regime.~~ Shallow PS generally exhibit narrow distributions of both D_m and N_w , particularly in high-latitude shallow
563 PS. Among the strong PS, those with a higher land proportion exhibit a narrower distribution of N_w values, whereas those
564 with a greater ocean proportion exhibit larger N_w values. However, the behavior of D_m is opposite: PS with a higher ocean
565 proportion show a narrower distribution of D_m values than land-dominated PS.~~Among the strong PS, PS with a higher land~~
566 ~~proportion exhibit more concentrated N_w values, whereas those with a greater ocean proportion exhibit larger N_w values.~~
567 ~~However, the distribution of D_m is the opposite: PS with a higher ocean proportion exhibit more concentrated D_m values than~~
568 ~~land-dominated PSs do.~~

569

570 4). The different PS exhibit distinct microphysical processes. In shallow convective PS, such as subtropical shallow PS and
571 high-latitude shallow PS, coalescence processes largely shape the microphysical characteristics, indicating the aggregation of
572 small raindrops in these PS. In contrast, extreme PSsPS are characterized by balanced breakup and coalescence processes,
573 highlighting a more complex interaction between raindrop formation and breakup. These results emphasize the varying
574 mechanisms that govern microphysical behavior across the different types of PSsPS. PS types with high precipitation rates are
575 dominated primarily by balanced breakup and coalescence processes, whereas shallow PSsPS are characterized mainly by
576 coalescence.

577

578 5). The seasonal and diurnal cycles of PSsPS and their microphysical parameters vary across clusters. Continental convection
579 clusters peak in the afternoon and summer~~Continental convection Cluster peak in the afternoon and summer~~, whereas tropical
580 and high-latitude systems exhibit unique seasonal and diurnal cycles, often with opposite trends between D_m and N_w .

581

582 Classifying PS is essential for increasing the understanding of the microphysical processes that govern cloud development and
583 precipitation formation across various climatic regimes. This classification enables the identification of key mechanisms that
584 shape precipitation particle formation, growth, and distribution, thereby providing a more physically grounded view of
585 precipitation system diversity.~~This classification enables the identification of specific mechanisms that influence rainfall~~
586 ~~characteristics, such as droplet formation, growth, and distribution, which are vital for accurate weather predictions and climate~~
587 ~~modeling.~~ This study revealed the global distribution characteristics of different types of PS and elucidated the variations in
588 microphysical properties across regions with distinct climatic and geographic conditions. Among the findings, the identified
589 PS types are closely linked to consistent variations in key microphysical parameters, suggesting that this objective
590 classification framework can effectively distinguish precipitation regimes with different underlying physical mechanisms.
591 These results provide new observational evidence for global precipitation variability and establish a physically consistent
592 framework for process-oriented comparisons, cross-regional analyses, and the evaluation of satellite precipitation products and
593 numerical model representations of precipitation systems.

594

595 ~~In this study, each PS was treated as integrated entity, without considering the variations in D_m and N_w within each system.~~
596 ~~Microphysical properties can vary significantly at the pixel level, and relying solely on average or maximum D_m and N_w values~~
597 ~~captures only part of the overall process. Future work should focus on analyzing pixel level observations to better understand~~
598 ~~the characteristics of microphysical parameters within PS. Moreover, the melting layer height was not explicitly considered,~~
599 ~~which limits the interpretation of vertical variations across the melting layer. Future work should incorporate pixel level~~
600 ~~observations and melting layer characteristics to better understand the microphysical features within PSs. Furthermore,~~
601 ~~investigating the relationships between microphysical parameters and convective parameters will be a key focus of future~~
602 ~~research. It should also be noted that the DPR is not particularly suitable for quantifying extreme precipitation rates. In heavy~~
603 ~~precipitation, Ku and Ka band signals are strongly affected by attenuation and multiple scattering, which can lead to~~

604 ~~underestimation of radar reflectivity and the associated precipitation rates (Battaglia et al., 2014). Therefore, no further~~
605 ~~discussion of extreme rain rates is provided in this study. We hope that future studies can develop improved precipitation~~
606 ~~retrieval algorithms to address this issue. By analyzing the interactions between these parameters, it is possible to reveal the~~
607 ~~influences of microphysical characteristics on convective intensity and precipitation patterns, providing a more detailed~~
608 ~~perspective for accurately predicting and understanding precipitation phenomena.~~

609

610 **Data Availability.** The GPM-DPR (version 07A) data from the NASA/Goddard Space Flight Center are available at
611 https://disc.gsfc.nasa.gov/datasets/GPM_2A-DPR_07/summary. All statistics and visualization are operated with Anaconda
612 Individual Edition Python version 3.8.3 (Free Download | Anaconda, accessed on 10 April 2022).

613

614 **Author contributions.** XZ and XN conceptualised and planned the research study. XZ conducted the satellite data analysis
615 with support from XN and drafted the initial manuscript. XN and JZ reviewed and revised the manuscript to refine its content.

616

617 **Competing interests.** The contact author has declared that none of the authors has any competing interests.

618

619 **Financial support.** This study is supported by the National Natural Science Foundation of China (42105005), Fundamental
620 Research Funds for the Central Universities (SWU-KT22007), and General Program of Chongqing Natural Science
621 Foundation (2022NSCQ-MSX3145).

622

623 **References**

624 Arulraj, M. and Barros, A. P.: Automatic detection and classification of low-level orographic precipitation processes from
625 space-borne radars using machine learning, *Remote Sensing of Environment*, 257, 112355,
626 <https://doi.org/10.1016/j.rse.2021.112355>, 2021.

627 Awaka, J., Le, M., Brodzik, S., Kubota, T., Masaki, T., Chandrasekar, V., and Iguchi, T.: Development of precipitation type
628 classification algorithms for a full scan mode of GPM dual-frequency precipitation radar, *Journal of the Meteorological Society*
629 of Japan. Ser. II, 99, 1253–1270, <https://doi.org/10.2151/jmsj.2021-061>, 2021.

630 Ay, M., Özbakır, L., Kulluk, S., Gülmez, B., Öztürk, G., and Özer, S.: FC-Kmeans: Fixed-centered K-means algorithm, *Expert*
631 *Systems with Applications*, 211, 118656, <https://doi.org/10.1016/j.eswa.2022.118656>, 2023.

632 Bang, S. D. and Cecil, D. J.: Testing Passive Microwave-Based Hail Retrievals Using GPM DPR Ku-Band Radar, *Journal of*
633 *Applied Meteorology and Climatology*, 60, 255–271, <https://doi.org/10.1175/JAMC-D-20-0129.1>, 2021.

634 Becker, T. and Hohenegger, C.: Entrainment and its dependency on environmental conditions and convective organization in
635 convection-permitting simulations, *Monthly Weather Review*, 149, 537–550, <https://doi.org/10.1175/MWR-D-20-0229.1>,
636 2021.

637 Bringi, V. N., Chandrasekar, V., Hubbert, J., Gorgucci, E., Randeu, W. L., and Schoenhuber, M.: Raindrop size distribution
638 in different climatic regimes from disdrometer and dual-polarized radar analysis, *Journal of the Atmospheric Sciences*, 60,
639 354–365, [https://doi.org/10.1175/1520-0469\(2003\)060<0354:RSDIDC>2.0.CO;2](https://doi.org/10.1175/1520-0469(2003)060<0354:RSDIDC>2.0.CO;2), 2003.

640 Cha, J. W. and Yum, S. S.: Characteristics of Precipitation Particles Measured by PARSIVEL Disdrometer at a Mountain and
641 a Coastal Site in Korea, *Asia-Pacific J Atmos Sci*, 57, 261–276, <https://doi.org/10.1007/s13143-020-00190-6>, 2021.

642 Chase, R. J., Nesbitt, S. W., and McFarquhar, G. M.: Evaluation of the Microphysical Assumptions within GPM-DPR Using
643 Ground-Based Observations of Rain and Snow, *Atmosphere*, 11, 619, <https://doi.org/10.3390/atmos11060619>, 2020.

644 Chen, B. and Liu, C.: Warm organized rain systems over the tropical eastern Pacific, *Journal of Climate*, 29, 3403–3422,
645 <https://doi.org/10.1175/JCLI-D-15-0177.1>, 2016.

646 Chen, B., Hu, W., and Pu, J.: Characteristics of the raindrop size distribution for freezing precipitation observed in southern
647 China, *Journal of Geophysical Research: Atmospheres*, 116, <https://doi.org/10.1029/2010JD015305>, 2011.

648 Chudler, K., Rutledge, S. A., and Dolan, B.: Unique radar observations of large raindrops in tropical warm rain during PISTON,
649 *Monthly Weather Review*, 150, 2719–2736, <https://doi.org/10.1175/MWR-D-21-0298.1>, 2022.

650 D’Adderio, L. P., Vulpiani, G., Porcù, F., Tokay, A., and Meneghini, R.: Comparison of GPM Core Observatory and Ground-
651 Based Radar Retrieval of Mass-Weighted Mean Raindrop Diameter at Midlatitude, *Journal of Hydrometeorology*, 19, 1583–
652 1598, <https://doi.org/10.1175/JHM-D-18-0002.1>, 2018.

653 Dai, Q., Zhu, J., Zhang, S., Zhu, S., Han, D., and Lv, G.: Estimation of rainfall erosivity based on WRF-derived raindrop size
654 distributions, *Hydrology and Earth System Sciences*, 24, 5407–5422, <https://doi.org/10.5194/hess-24-5407-2020>, 2020.

655 Das, S. and Chatterjee, C.: Rain characterization based on maritime and continental origin at a tropical location, *Journal of*
656 *Atmospheric and Solar-Terrestrial Physics*, 173, 109–118, <https://doi.org/10.1016/j.jastp.2018.02.011>, 2018.

657 Das, S., Wang, Y., Gong, J., Ding, L., Munchak, S. J., Wang, C., Wu, D. L., Liao, L., Olson, W. S., and Barahona, D. O.: A
658 comprehensive machine learning study to classify precipitation type over land from Global Precipitation Measurement
659 Microwave Imager (GPM-GMI) measurements, *Remote Sensing*, 14, 3631, <https://doi.org/10.3390/rs14153631>, 2022.

660 Dolan, B., Fuchs, B., Rutledge, S. A., Barnes, E. A., and Thompson, E. J.: Primary modes of global drop size distributions,
661 *Journal of the Atmospheric Sciences*, 75, 1453–1476, <https://doi.org/10.1175/JAS-D-17-0242.1>, 2018.

662 El Khattabi, M.-Z., El Jai, M., Lahmadi, Y., Oughdir, L., and Rahhali, M.: Understanding the Interplay Between Metrics,
663 Normalization Forms, and Data distribution in K-Means Clustering: A Comparative Simulation Study, *Arab J Sci Eng*, 49,
664 2987–3007, <https://doi.org/10.1007/s13369-023-07741-9>, 2024.

665 Festa, D., Novellino, A., Hussain, E., Bateson, L., Casagli, N., Confuorto, P., Del Soldato, M., and Raspini, F.: Unsupervised
666 detection of InSAR time series patterns based on PCA and K-means clustering, *International Journal of Applied Earth*
667 *Observation and Geoinformation*, 118, 103276, <https://doi.org/10.1016/j.jag.2023.103276>, 2023.

668 Gang, A. and Bajwa, W. U.: FAST-PCA: A Fast and Exact Algorithm for Distributed Principal Component Analysis, IEEE
669 Transactions on Signal Processing, 70, 6080–6095, <https://doi.org/10.1109/TSP.2022.3229635>, 2022.

670 Gatlin, P. N., Petersen, W. A., Pippitt, J. L., Berendes, T. A., Wolff, D. B., and Tokay, A.: The GPM Validation Network and
671 Evaluation of Satellite-Based Retrievals of the Rain Drop Size Distribution, Atmosphere, 11,
672 <https://doi.org/10.3390/atmos11091010>, 2020.

673 Gupta, A. K., Deshmukh, A., Waman, D., Patade, S., Jadav, A., Phillips, V. T. J., Bansemmer, A., Martins, J. A., and Gonçalves,
674 F. L. T.: The microphysics of the warm-rain and ice crystal processes of precipitation in simulated continental convective
675 storms, Commun Earth Environ, 4, 226, <https://doi.org/10.1038/s43247-023-00884-5>, 2023.

676 Hamada, A., Takayabu, Y. N., Liu, C., and Zipser, E. J.: Weak linkage between the heaviest rainfall and tallest storms, Nature
677 Communications, 6, 6213, <https://doi.org/10.1038/ncomms7213>, 2015.

678 Hou, A. Y., Kakar, R. K., Neeck, S., Azarbarzin, A. A., Kummerow, C. D., Kojima, M., Oki, R., Nakamura, K., and Iguchi,
679 T.: The global precipitation measurement mission, Bulletin of the American Meteorological Society, 95, 701–722,
680 <https://doi.org/10.1175/BAMS-D-13-00164.1>, 2014.

681 Houze Jr., R. A., Rasmussen, K. L., Zuluaga, M. D., and Brodzik, S. R.: The variable nature of convection in the tropics and
682 subtropics: A legacy of 16 years of the Tropical Rainfall Measuring Mission satellite, Reviews of Geophysics, 53, 994–1021,
683 <https://doi.org/10.1002/2015RG000488>, 2015.

684 Hu, X., Ai, W., Qiao, J., and Yan, W.: Insight into global climatology of melting layer: latitudinal dependence and orographic
685 relief, Theor Appl Climatol, 155, 4863–4873, <https://doi.org/10.1007/s00704-024-04926-6>, 2024.

686 Huang, H., Zhao, K., Fu, P., Chen, H., Chen, G., and Zhang, Y.: Validation of Precipitation Measurements From the Dual-
687 Frequency Precipitation Radar Onboard the GPM Core Observatory Using a Polarimetric Radar in South China, IEEE
688 Transactions on Geoscience and Remote Sensing, 60, 1–16, <https://doi.org/10.1109/TGRS.2021.3118601>, 2022.

689 Iguchi, T., Kozu, T., Meneghini, R., Awaka, J., and Okamoto, K.: Rain-Profiling algorithm for the TRMM precipitation radar,
690 Journal of Applied Meteorology and Climatology, 39, 2038–2052, <https://doi.org/10.1175/1520->
691 0450(2001)040<2038:RPAFTT>2.0.CO;2, 2000.

692 Iguchi, T., Seto, S., Meneghini, R., Yoshida, N., Awaka, J., Le, M., Chandrasekar, V., Brodzik, S., Tanelli, S., Kanemaru, K.,
693 Masaki, T., Kubota, T., and Takahashi, N.: GPM/DPR Level-2 Algorithm Theoretical Basis Document, 2021.

694 Jain, A. K.: Data clustering: 50 years beyond K-means, Pattern Recognition Letters, 31, 651–666,
695 <https://doi.org/10.1016/j.patrec.2009.09.011>, 2010.

696 Jiang, H.: The relationship between tropical cyclone intensity change and the strength of inner-core convection, Monthly
697 Weather Review, 140, 1164–1176, <https://doi.org/10.1175/MWR-D-11-00134.1>, 2012.

698 Jolliffe, I. T. and Cadima, J.: Principal component analysis: a review and recent developments, Philosophical Transactions of
699 the Royal Society A: Mathematical, Physical and Engineering Sciences, 374, 20150202,
700 <https://doi.org/10.1098/rsta.2015.0202>, 2016.

701 Kumar, K. S., Das, S. K., Deshpande, S. M., Deshpande, M., and Pandithurai, G.: Regional variability of precipitation
702 characteristics in tropical cyclones over the North Indian Ocean from GPM-DPR measurements, *Atmospheric Research*, 283,
703 106568, <https://doi.org/10.1016/j.atmosres.2022.106568>, 2023.

704 Kumar, S., Flores-Rojas, J. L., Moya-Álvarez, A. S., Martínez-Castro, D., and Silva, Y.: Hydrometeors distribution in intense
705 precipitating cloud cells over the earth's during two rainfall seasons, *J Indian Soc Remote Sens*, 52, 95–111,
706 <https://doi.org/10.1007/s12524-023-01805-x>, 2024.

707 Kumjian, M. R. and Prat, O. P.: The impact of raindrop collisional processes on the polarimetric radar variables, *Journal of the*
708 *Atmospheric Sciences*, 71, 3052–3067, <https://doi.org/10.1175/JAS-D-13-0357.1>, 2014.

709 Lerber, A. von, Moisseev, D., Marks, D. A., Petersen, W., Harri, A.-M., and Chandrasekar, V.: Validation of GMI Snowfall
710 Observations by Using a Combination of Weather Radar and Surface Measurements, *Journal of Applied Meteorology and*
711 *Climatology*, 57, 797–820, <https://doi.org/10.1175/JAMC-D-17-0176.1>, 2018.

712 Li, D., Qi, Y., and Li, H.: Statistical characteristics of convective and stratiform precipitation during the rainy season over
713 South China based on GPM-DPR observations, *Atmospheric Research*, 301, 107267,
714 <https://doi.org/10.1016/j.atmosres.2024.107267>, 2024.

715 Liu, C.: Rainfall Contributions from Precipitation Systems with Different Sizes, Convective Intensities, and Durations over
716 the Tropics and Subtropics, *Journal of Hydrometeorology*, 12, 394–412, <https://doi.org/10.1175/2010JHM1320.1>, 2011.

717 Liu, C. and Zipser, E. J.: The global distribution of largest, deepest, and most intense precipitation systems, *Geophysical*
718 *Research Letters*, 42, 3591–3595, <https://doi.org/10.1002/2015GL063776>, 2015.

719 Liu, C., Zipser, E. J., and Nesbitt, S. W.: Global Distribution of Tropical Deep Convection: Different Perspectives from TRMM
720 Infrared and Radar Data, <https://doi.org/10.1175/JCLI4023.1>, 2007.

721 Liu, C., Zipser, E. J., Cecil, D. J., Nesbitt, S. W., and Sherwood, S.: A cloud and precipitation feature database from nine years
722 of TRMM observations, *Journal of Applied Meteorology and Climatology*, 47, 2712–2728,
723 <https://doi.org/10.1175/2008JAMC1890.1>, 2008.

724 Liu, N., Liu, C., and Hayden, L.: Climatology and detection of overshooting convection from 4 years of GPM precipitation
725 radar and passive microwave observations, *Journal of Geophysical Research: Atmospheres*, 125, e2019JD032003,
726 <https://doi.org/10.1029/2019JD032003>, 2020.

727 Marukatat, S.: Tutorial on PCA and approximate PCA and approximate kernel PCA, *Artif Intell Rev*, 56, 5445–5477,
728 <https://doi.org/10.1007/s10462-022-10297-z>, 2023.

729 Marzuki, M., Ramadhan, R., Yusnaini, H., Renggono, F., Vonnisa, M., and Hashiguchi, H.: Comparison of vertical profile of
730 raindrop size distribution from micro rain radar with global precipitation measurement over Western Java Island, *Remote*
731 *Sensing Applications: Society and Environment*, 29, 100885, <https://doi.org/10.1016/j.rsase.2022.100885>, 2023.

732 Mroz, K., Battaglia, A., and Fridlind, A. M.: Enhancing consistency of microphysical properties of precipitation across the
733 melting layer in dual-frequency precipitation radar data, *Atmospheric Measurement Techniques*, 17, 1577–1597,
734 <https://doi.org/10.5194/amt-17-1577-2024>, 2024.

735 Ni, X., Liu, C., Cecil, D. J., and Zhang, Q.: On the detection of hail Using satellite passive microwave radiometers and
736 precipitation radar, *Journal of Applied Meteorology and Climatology*, 56, 2693–2709, [https://doi.org/10.1175/JAMC-D-17-](https://doi.org/10.1175/JAMC-D-17-0065.1)
737 0065.1, 2017.

738 Ni, X., Liu, C., and Zipser, E.: Ice microphysical properties near the tops of deep convective cores implied by the GPM Dual-
739 Frequency Radar observations, *Journal of the Atmospheric Sciences*, 76, 2899–2917, [https://doi.org/10.1175/JAS-D-18-](https://doi.org/10.1175/JAS-D-18-0243.1)
740 0243.1, 2019.

741 Peinó, E., Bech, J., Polls, F., Udina, M., Petracca, M., Adirosi, E., Gonzalez, S., and Boudevillain, B.: Validation of GPM DPR
742 Rainfall and Drop Size Distributions Using Disdrometer Observations in the Western Mediterranean, *Remote Sensing*, 16,
743 2594, <https://doi.org/10.3390/rs16142594>, 2024.

744 Roy, P., Biswasharma, R., Deshamukhya, A., and Sharma, S.: Spatial and seasonal variation of rainfall contribution by the
745 height spectrum of precipitation systems and associated cloud bulk properties over the South Asia, *International Journal of*
746 *Climatology*, 40, 3771–3791, <https://doi.org/10.1002/joc.6427>, 2020.

747 Saha, P., Majumder, S., and Maitra, A.: Rain drop size distribution analysis at a tropical location near land-sea boundary,
748 *Theor Appl Climatol*, 147, 487–498, <https://doi.org/10.1007/s00704-021-03809-4>, 2022.

749 Seela, B. K., Janapati, J., Lin, P.-L., Wang, P. K., and Lee, M.-T.: Raindrop size distribution characteristics of summer and
750 winter season rainfall over North Taiwan, *Journal of Geophysical Research: Atmospheres*, 123, 11,602–11,624,
751 <https://doi.org/10.1029/2018JD028307>, 2018.

752 Seela, B. K., Janapati, J., Lin, P.-L., Lan, C.-H., and Huang, M.-Q.: Evaluation of GPM DPR Rain Parameters with North
753 Taiwan Disdrometers, <https://doi.org/10.1175/JHM-D-23-0027.1>, 2023.

754 Shi, R., Lu, C., Xu, W., and Luo, Y.: A global view on microphysical discriminations between heavier and lighter convective
755 rainfall, *Commun Earth Environ*, 6, 511, <https://doi.org/10.1038/s43247-025-02473-0>, 2025.

756 Skofronick-Jackson, G., Petersen, W. A., Berg, W., Kidd, C., Stocker, E. F., Kirschbaum, D. B., Kakar, R., Braun, S. A.,
757 Huffman, G. J., Iguchi, T., Kirstetter, P. E., Kummerow, C., Meneghini, R., Oki, R., Olson, W. S., Takayabu, Y. N., Furukawa,
758 K., and Wilheit, T.: The global precipitation measurement (GPM) mission for science and society, *Bulletin of the American*
759 *Meteorological Society*, 98, 1679–1695, <https://doi.org/10.1175/BAMS-D-15-00306.1>, 2017.

760 Snook, N. and Xue, M.: Effects of microphysical drop size distribution on tornadogenesis in supercell thunderstorms,
761 *Geophysical Research Letters*, 35, <https://doi.org/10.1029/2008GL035866>, 2008.

762 Sowan, B., Hong, T.-P., Al-Qerem, A., Alauthman, M., and Matar, N.: Ensembling validation indices to estimate the optimal
763 number of clusters, *Appl Intell*, 53, 9933–9957, <https://doi.org/10.1007/s10489-022-03939-w>, 2023.

764 Suh, S.-H., You, C.-H., and Lee, D.-I.: Climatological characteristics of raindrop size distributions in Busan, Republic of Korea,
765 *Hydrology and Earth System Sciences*, 20, 193–207, <https://doi.org/10.5194/hess-20-193-2016>, 2016.

766 Sun, Y., Dong, X., Cui, W., Zhou, Z., Fu, Z., Zhou, L., Deng, Y., and Cui, C.: Vertical Structures of Typical Meiyu
767 Precipitation Events Retrieved From GPM-DPR, *Journal of Geophysical Research: Atmospheres*, 125, e2019JD031466,
768 <https://doi.org/10.1029/2019JD031466>, 2020.

769 Tapiador, F. J., Turk, F. J., Petersen, W., Hou, A. Y., García-Ortega, E., Machado, L. A. T., Angelis, C. F., Salio, P., Kidd, C.,
770 Huffman, G. J., and de Castro, M.: Global precipitation measurement: Methods, datasets and applications, *Atmospheric*
771 *Research*, 104–105, 70–97, <https://doi.org/10.1016/j.atmosres.2011.10.021>, 2012.

772 Thompson, E. J., Rutledge, S. A., Dolan, B., and Thurai, M.: Drop size distributions and radar observations of convective and
773 stratiform rain over the equatorial Indian and west Pacific Oceans, *Journal of the Atmospheric Sciences*, 72, 4091–4125,
774 <https://doi.org/10.1175/JAS-D-14-0206.1>, 2015.

775 Uma, K. N. and Rao, T. N.: Characteristics of vertical velocity cores in different convective systems observed over Gadanki,
776 India, *Monthly Weather Review*, 137, 954–975, <https://doi.org/10.1175/2008MWR2677.1>, 2009.

777 Wang, T. and Tang, G.: Spatial Variability and Linkage Between Extreme Convections and Extreme Precipitation Revealed
778 by 22-Year Space-Borne Precipitation Radar Data, *Geophysical Research Letters*, 47, e2020GL088437,
779 <https://doi.org/10.1029/2020GL088437>, 2020.

780 Wen, J., Wang, G., Zhou, R., Li, R., Zhaxi, S., and Bai, M.: Seasonal Variation in Vertical Structure for Stratiform Rain at
781 Mêdog Site in Southeastern Tibetan Plateau, *Remote Sensing*, 16, 1230, <https://doi.org/10.3390/rs16071230>, 2024.

782 Wen, L., Chen, G., Yang, C., Zhang, H., and Fu, Z.: Seasonal variations in precipitation microphysics over East China based
783 on GPM DPR observations, *Atmospheric Research*, 293, 106933, <https://doi.org/10.1016/j.atmosres.2023.106933>, 2023.

784 Wu, Z., Zhang, Y., Zhang, L., Zheng, H., and Huang, X.: A comparison of convective and stratiform precipitation microphysics
785 of the record-breaking typhoon In-Fa (2021), *Remote Sensing*, 14, 344, <https://doi.org/10.3390/rs14020344>, 2022.

786 Zhang, Y. and Wang, K.: Global precipitation system size, *Environ. Res. Lett.*, 16, 054005, [https://doi.org/10.1088/1748-](https://doi.org/10.1088/1748-9326/abf394)
787 [9326/abf394](https://doi.org/10.1088/1748-9326/abf394), 2021.

788 Zhang, Z., Li, H., Li, D., and Qi, Y.: Spatial variability of raindrop size distribution at Beijing city scale and its implications
789 for polarimetric radar QPE, *Remote Sensing*, 15, 3964, <https://doi.org/10.3390/rs15163964>, 2023.

790 Zipser, E. J., Cecil, D. J., Liu, C., Nesbitt, S. W., and Yorty, D. P.: WHERE ARE THE MOST INTENSE THUNDERSTORMS
791 ON EARTH?, *Bull. Amer. Meteor. Soc.*, 87, 1057–1072, <https://doi.org/10.1175/BAMS-87-8-1057>, 2006.

792